Cell Reports

Article

Mitochondrial hyperfusion via metabolic sensing of regulatory amino acids

Graphical abstract

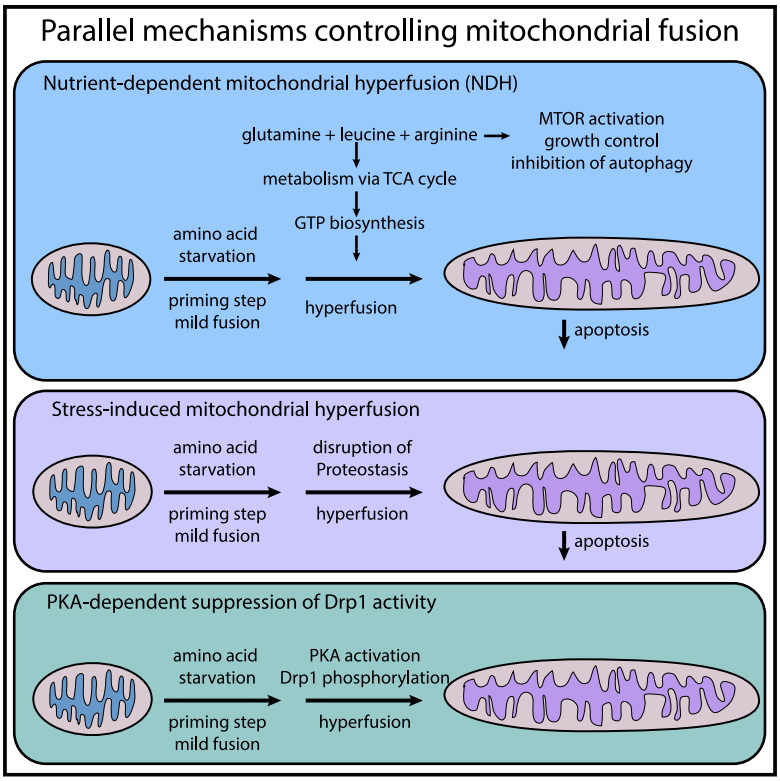

Highlights

- Regulatory amino acids glutamine, leucine, and arginine drive mitochondrial hyperfusion
- Cellular amino acids are sensed in a MTORC1-independent manner
- Glutamine is metabolized to fuel TCA intermediates and GTP biosynthesis
- Nutrient-dependent mitochondrial hyperfusion controls apoptosis

Authors

Mahmud O. Abdullah, Run X. Zeng, Chelsea L. Margerum, ..., Daina Avizonis, Ivan Topisirovic, Edmond Y.W. Chan

Correspondence

eywc@queensu.ca

In brief

Abdullah et al. reveal that a metabolic pathway can sense levels of amino acids glutamine, leucine, and arginine to drive mitochondrial hyperfusion. This nutrient-sensing pathway does not require MTORC1 but is dependent upon the TCA cycle and purine biogenesis. Nutrient-dependent mitochondrial hyperfusion can go on to regulate cell fate.

Abdullah et al., 2022, Cell Reports *40*, 111198
August 16, 2022
https://doi.org/10.1016/j.celrep.2022.111198

CellPress

Cell Reports

CellPress
OPEN ACCESS

Article

Mitochondrial hyperfusion via metabolic sensing of regulatory amino acids

Mahmud O. Abdullah,[1] Run X. Zeng,[2] Chelsea L. Margerum,[2] David Papadopoli,[3] Cian Monnin,[4] Kaylee B. Punter,[2] Charles Chu,[2] Mohammad Al-Rofaidi,[1] Naser F. Al-Tannak,[1,5] Domenica Berardi,[1] Zahra Rattray,[1] Nicholas J.W. Rattray,[1] Sheela A. Abraham,[2] Eeva-Liisa Eskelinen,[6] David G. Watson,[1] Daina Avizonis,[4] Ivan Topisirovic,[3] and Edmond Y.W. Chan[1,2,7,*]

[1]Strathclyde Institute for Pharmacy and Biomedical Sciences, University of Strathclyde, Glasgow, Scotland
[2]Department of Biomedical and Medical Sciences, Queen's University, Kingston, Canada
[3]Lady Davis Institute, Gerald Bronfman Department of Oncology, Department of Biochemistry, Department of Experimental Medicine, McGill University, Montreal, Canada
[4]Metabolomics Innovation Resource, Rosalind and Morris Goodman Cancer Institute, McGill University, Montreal, Canada
[5]Department of Pharmaceutical Chemistry, Faculty of Pharmacy, Kuwait University, Kuwait City, Kuwait
[6]Institute of Biomedicine, University of Turku, Turku, Finland
[7]Lead contact
*Correspondence: eywc@queensu.ca
https://doi.org/10.1016/j.celrep.2022.111198

SUMMARY

The relationship between nutrient starvation and mitochondrial dynamics is poorly understood. We find that cells facing amino acid starvation display clear mitochondrial fusion as a means to evade mitophagy. Surprisingly, further supplementation of glutamine (Q), leucine (L), and arginine (R) did not reverse, but produced stronger mitochondrial hyperfusion. Interestingly, the hyperfusion response to Q + L + R was dependent upon mitochondrial fusion proteins Mfn1 and Opa1 but was independent of MTORC1. Metabolite profiling indicates that Q + L + R addback replenishes amino acid and nucleotide pools. Inhibition of fumarate hydratase, glutaminolysis, or inosine monophosphate dehydrogenase all block Q + L + R-dependent mitochondrial hyperfusion, which suggests critical roles for the tricarboxylic acid (TCA) cycle and purine biosynthesis in this response. Metabolic tracer analyses further support the idea that supplemented Q promotes purine biosynthesis by serving as a donor of amine groups. We thus describe a metabolic mechanism for direct sensing of cellular amino acids to control mitochondrial fusion and cell fate.

INTRODUCTION

Mitochondria display remarkably dynamic membrane remodeling that reflects their origin as autonomous bacteria (Dyall et al., 2004; Westermann, 2010). This enormous flexibility appears critical to sustain bioenergetics, particularly in metabolically demanding cells such as neurons, and may allow cancer cells to shift fuel utilization during starvation conditions (Nagdas et al., 2019). In normal contexts, new mitochondria are formed by expansion of existing organelles followed by fission to form progeny. Mitochondrial fission is promoted by dynamin-related protein 1 (Drp1), which localizes to the mitochondrial membrane via adaptor proteins to form ring structures that drive scission in a GTP-dependent manner (Lackner et al., 2009). Drp1 can be negatively regulated by phosphorylation at S637 via protein kinase A (PKA), which causes dissociation from mitochondria (Cereghetti et al., 2008; Cribbs and Strack, 2007). Other post-translational mechanisms include Drp1 SUMOylation and phosphorylation at S616, which are both associated with increased fission (Kashatus et al., 2015; Prudent et al., 2015; Serasinghe et al., 2015; Taguchi et al., 2007). Drp1-mediated fission is essential at the cellular level for mitochondrial propagation during mitosis, as seen from knockout (KO) evidence during mammalian embryogenesis (Ishihara et al., 2009; Taguchi et al., 2007; Wakabayashi et al., 2009). Fission facilitates cytochrome *c* release from mitochondria and can therefore modulate levels of apoptosis (Frank et al., 2001; Prudent et al., 2015; Pyakurel et al., 2015; Wasiak et al., 2007). Importantly, Drp1-mediated fission is critical for quality control and homeostatic clearance via mitophagy (Kleele et al., 2021; Twig et al., 2008), potentially by directing specific capture of damaged mitochondrial regions by autophagosomes (Burman et al., 2017).

Counteracting fission, mitochondria constantly undergo fusion, leading to a dynamic interplay between the two opposing pathways (Nunnari et al., 1997). Fusion of the outer mitochondrial membrane is directed by mitofusin1 (Mfn1) together with mitochondria-endoplasmic reticulum tethering factor (Mfn2) (Chen et al., 2003; Naon et al., 2016), while inner membrane fusion is directed by optic atrophy 1 (Opa1) (Ishihara et al., 2006). Multiple mechanisms have been described to regulate these fusion factors, including phosphorylation or redox state (for Mfn1/2) (Chen and Dorn, 2013; Leboucher et al., 2012; Pyakurel et al.,

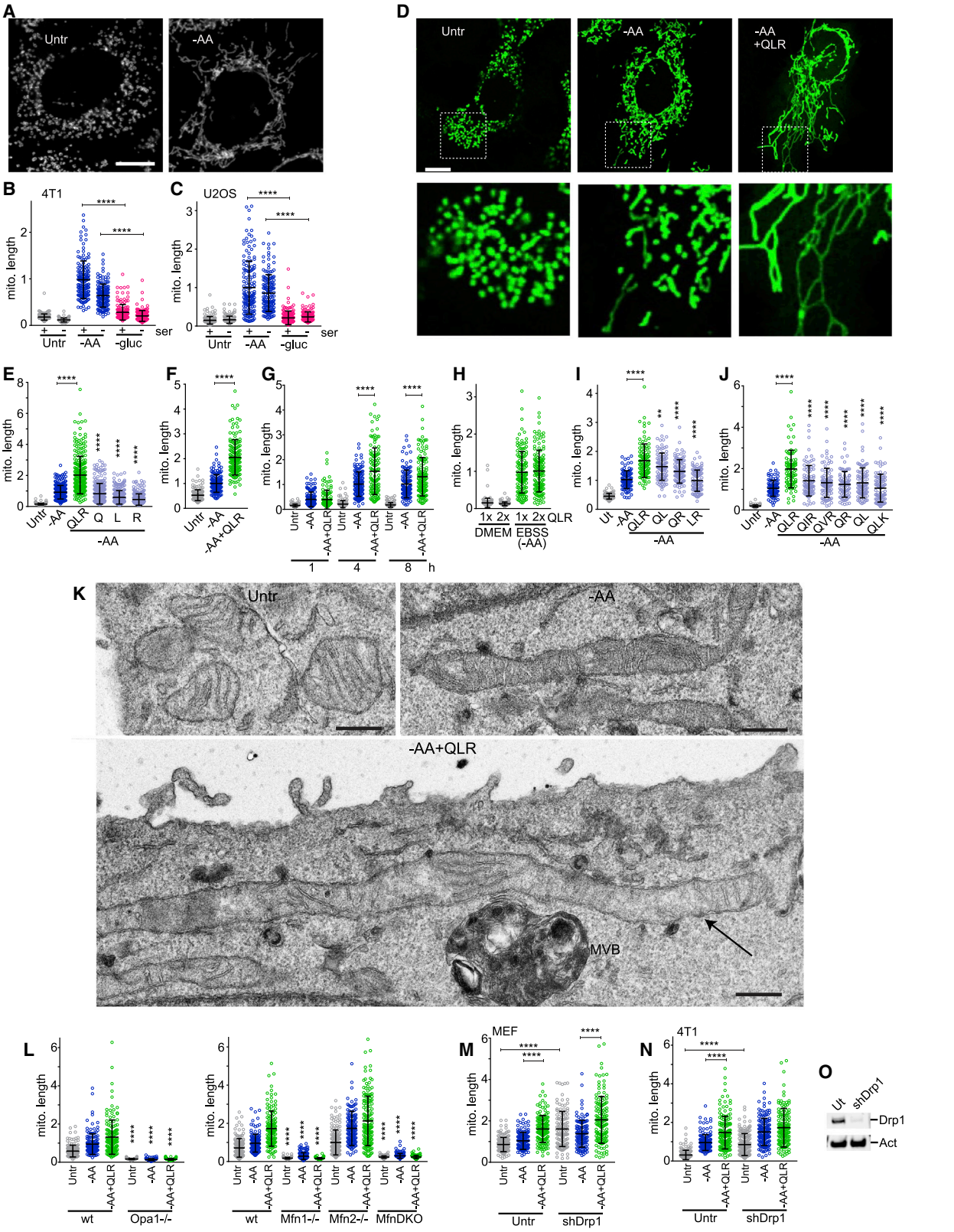

(legend on next page)

2015; Shutt et al., 2012) and proteolytic processing (for Opa1) (Head et al., 2009; Ishihara et al., 2006; Mishra et al., 2014). Interestingly, fusion has been proposed to critically maintain mitochondrial function by facilitating content mixing, thereby providing complementation for mtDNA mutations (Nakada et al., 2001; Ono et al., 2001), or by sustaining mitochondrial fitness to suppress mtDNA deterioration (Chen et al., 2007, 2010). Timely coordination of fission and fusion has been shown to be critical for progression through the cell cycle, to potentially permit eventual distribution of small mitochondria to daughter cells (Mitra et al., 2009). A stress-induced mitochondrial hyperfusion (SIMH) pathway has also been described to drive formation of interconnected networks as an adaptive response to multiple stress conditions such as UV irradiation or inhibition of protein synthesis (Lebeau et al., 2018; Tondera et al., 2009). Overall, mitochondrial fusion is a positive contributor of functional robustness under a number of different contexts, including cellular aging and resistance to cell death (Miret-Casals et al., 2018; Sun et al., 2016).

Here, we aimed to understand how mitochondrial dynamics respond to nutrient cues following our previous work on regulation of autophagy and lysosomal function (Gallagher et al., 2017; Nwadike et al., 2018). We were intrigued by previous studies that demonstrated how mitochondria undergo fusion following nutrient starvation stress, thereby generating large networks that escape mitophagy to sustain bioenergetics (Gomes et al., 2011a; Rambold et al., 2011a). Accordingly, we investigated nutrient signals controlling mitochondrial fusion, focusing on amino acids that play predominant signaling roles upstream of mechanistic target of rapamycin complex 1 (MTORC1) and autophagy (Nwadike et al., 2018). Unexpectedly, addback of regulatory amino acids (glutamine [Q] + leucine [L] + arginine [R]) promoted further mitochondrial hyperfusion, which required downstream metabolic pathways but was independent of the MTORC1 central nutrient-sensing pathway. Our results therefore establish a metabolic mechanism that links amino acid sensing to mitochondrial dynamics that works in parallel with other stress-dependent responses.

RESULTS

Amino-acid-dependent mitochondrial hyperfusion

To understand how mitochondria undergo nutrient-dependent remodeling, various forms of starvation were examined. Since we previously characterized nutrient-dependent modulation in 4T1 breast cancer cells (Gallagher et al., 2017), we continued using this model. We depleted levels of glucose or amino acids, both with and without serum starvation, and monitored mitochondrial morphology by staining for the outer membrane protein TOMM20. Resting 4T1 cells contained small-sized mitochondria and this was overall uniform within the cell population (Figures 1A and 1B). Serum starvation alone did not alter this basal phenotype. In contrast, following amino acid starvation, mitochondria remodeled toward increased fusion and a tubular state. Serum starvation only had small effects on mitochondrial fusion in the context of amino acid starvation. By comparison, starvation of glucose did not lead to robust mitochondrial fusion. We observed similar responses in U2OS (Figure 1C), RPE1, and HeLa cells (Figure S1A). Overall, mitochondrial fusion was most sensitive to depletion of amino acids.

A range of studies have established mechanisms for sensing intracellular amino acids, in particular Q, L, and R, upstream of MTORC1 (Chantranupong et al., 2016; Rebsamen et al., 2015). Interestingly, any single amino acid of these three is sufficient to stimulate MTORC1 (Carroll et al., 2016; Jewell et al., 2015),

Figure 1. Q, L, and R addback induces mitochondrial hyperfusion

(A) 4T1 cells were incubated under full nutrients as untreated control (Untr) or starved of amino acids (−AA) for 4 h. Mitochondria were visualized by staining TOMM20. Scale bar: 10 μm.

(B) Quantification of mitochondrial length in 4T1 cells starved of amino acid or glucose (−gluc) in combination with serum starvation. Each treatment shows 150 cells quantified from three experiments represented as arbitrary units relative to amino acid starvation (in presence of serum) as 1.

(C) Experiment in (B) tested using U2OS cells.

(D) 4T1/Su9GFP cells were incubated under full nutrients, starved of either all amino acids or incubated in starvation medium supplemented with Q, L, or R, or QLR together for 4 h. Scale bar: 10 μm. Zoomed insets shown below.

(E) Quantification of mitochondrial length in 4T1/Su9 cells. N = 250 cells from five experiments.

(F) Starvation conditions as in (E) tested in U2OS/Su9GFP cells. N = 200 cells; four experiments.

(G) 4T1/Su9GFP cells were incubated for the indicated times. N = 120 cells; three experiments. Arbitrary units relative to amino acid starvation (4 h) as 1.

(H) 4T1/Su9GFP cells were incubated in full-nutrient medium (DMEM) containing normal (1×) or double (2×) concentrations of QLR, or incubated in amino acid starvation medium (EBSS) containing 1× or 2× QLR. N = 120 cells; three experiments.

(I and J) 4T1/Su9GFP cells were incubated in amino acid starvation medium containing addback as indicated for 4 h. Each condition, N = 80–100 cells representing four experiments.

(K) 4T1/Su9GFP cells were incubated as indicated for 4 h and processed for electron microscopy. Scale bar: 400 nm. MVB, multivesicular body. Arrow indicates mitochondrion with amino-acid-dependent hyperfusion and disorganized cristae.

(L) Wild-type (wt) versus Opa1 (−/−) MEF, or matched wild-type versus Mfn1(−/−), Mfn2(−/−), or Mfn1/2 double-KO MEFs were starved as indicated for 4 h, assayed for mitochondrial fusion, and quantified in arbitrary units relative to amino acid starvation as 1. N = 150 cells; three experiments.

(M) MEF (wild type) stably expressed small hairpin RNA (shRNA) for Drp1 and were treated to starvation and QLR addback as indicated for 4 h. N = 150 cells; three experiments.

(N) 4T1 stably expressed Drp1 shRNA and were tested as in (C). N = 150 cells; three experiments.

(O) Knockdown confirmation for 4T1 cells.

Statistical comparisons were analyzed by one-way ANOVA with Bonferroni post tests as indicated. Statistical tests of single or alternate amino acid conditions (in E, I, and J) were performed relative to the QLR-addback condition. Statistical tests in (L) show comparisons of treatments in KO relative to corresponding condition in wt. ****$p < 0.0001$. All mitochondrial quantification plots show mean ± SD. All starvation medium conditions contained 10% dialyzed FBS (except in B and C).

but we previously found a stronger block of autophagy by addition of all three (Nwadike et al., 2018). Therefore, we tested if supplementation of Q, L, and R would reverse mitochondrial fusion responses. We treated 4T1/Su9GFP cells (expressing F0-ATPase subunit 9 fused to GFP) to starvation of all amino acids or to starvation medium supplemented with Q, L, and R. Surprisingly, supplementation of Q + L + R to the amino-acid-free medium led to hyperfused mitochondria with increased mitochondrial length (up to 3-fold longer relative to cells starved of all amino acids) (Figures 1D and 1E). Supplementation with either Q, L, or R (each singly) did not induce any hyperfusion above levels caused by general amino acid starvation. QLR-dependent hyperfusion was similarly observed in U2OS/Su9GFP cells (Figure 1F). Overall, addback of QLR to starvation medium led to mitochondrial hyperfusion, which was opposite to what we predicted.

The ability of QLR supplementation to promote hyperfusion could be detected within 1 h and could be sustained even after 8 h of starvation (Figure 1G). In the experiments above, Q, L, and R were supplemented into Earle's balanced salt solution (EBSS; an amino acid deprivation medium) to concentrations found in standard DMEM formulation. We found that addition of QLR to DMEM (such that these three amino acids were 2× normal concentration) did not induce any mitochondrial fusion. Interestingly, while addition of 1× concentrations of QLR into EBSS produced hyperfusion, 2× QLR concentrations failed to entice stronger effects (Figure 1H). These findings suggest that QLR-dependent mitochondrial hyperfusion requires the depletion of other amino acids.

Mitochondrial hyperfusion was next assessed by comparing supplementation of different amino acid combinations. While supplementation with Q + L + R induced extensive mitochondrial hyperfusion in 4T1/Su9GFP cells, supplementation of any two of these amino acids only induced moderate fusion (Figure 1I). Similar results were observed in U2OS/Su9GFP cells (Figure S1B). We further investigated if any amino acid replacements would alter QLR-dependent hyperfusion. To study branched-chain amino acids (BCAAs), we substituted L with valine or isoleucine. We also tested whether lysine (K) could substitute for R substitution in the addback mixture. We found that replacement with other BCAA in place of L reduced the extent of mitochondrial hyperfusion (Figure 1J). Replacement with K in place of R also reduced hyperfusion responses. In exploring further mixtures, we found that 2× concentrations of Q or R (but without L) were also not sufficient to promote maximal hyperfusion (Figure S1C). Overall, Q + L + R addback into the starvation medium has consistently provided the highest level of mitochondrial hyperfusion, suggesting that three amino acids are required at a balanced stoichiometry to drive mitochondrial membrane remodeling.

Role of canonical mitochondrial fusion machinery in amino-acid-dependent hyperfusion

To further characterize these events, we studied membrane ultrastructure during QLR-dependent mitochondrial hyperfusion. Untreated 4T1 cells predominantly contain smaller mitochondria with organized and regularly spaced cristae (Figure 1K). Upon amino acid starvation, cells showed fused mitochondria containing more irregular cristae. In contrast, cells treated to QLR-supplemented starvation medium contained dramatically hyperfused mitochondria, which also carried cristae that were disorganized, but often extended in length along the axis of the elongated mitochondria and without any bilayer swelling.

Since fusion of the outer and inner mitochondrial membranes are mediated by Mfn1/2 and Opa1, respectively, we wanted to clarify if these factors were involved during nutrient-dependent hyperfusion. Wild-type mouse embryonic fibroblasts (MEFs) in their basal state showed a more mixed mitochondria population relative to the more uniform size in 4T1 cells (Figures 1L left panel, S1D). Wild-type MEFs showed mild mitochondrial fusion following amino acid starvation and also displayed QLR-induced mitochondrial hyperfusion. On the other hand, Opa1 null MEFs (Song et al., 2007) showed small fragmented mitochondria in the basal state and were completely unresponsive to both starvation or QLR-dependent fusion. Interestingly, both mitochondrial fusion responses were also blocked in Mfn1 KO (Chen et al., 2003) and Mfn1/2 double-KO (null) MEFs (Koshiba et al., 2004) (Figures 1L right panel, S1E). In contrast, KO of Mfn2, which may be an ER-mitochondrial tethering factor, had no effect on nutrient-dependent mitochondrial fusion responses.

We also wished to determine if amino-acid-dependent hyperfusion was driven by a loss of mitochondrial fission. To address this, Drp1 was silenced in MEF (Figures 1M and S1F–S1H). In MEF, Drp1 silencing shifted the size distribution toward larger elongated mitochondria, consistent with an imbalance following loss of fission. Amino acid starvation of MEF/shDrp1 did not further drive mitochondrial fusion. However, treatment with starvation medium supplemented with QLR promoted hyperfusion in MEF/shDrp1. To further corroborate these findings, we tested the effects of Drp1 depletion in 4T1, which contain a more uniform population of small mitochondria (Figures 1N, 1O, and S1I). 4T1 cells also showed a clear shift toward fusion upon Drp1 silencing. In 4T1/shDrp1 cells, both amino acid starvation and further QLR supplementation promoted fusion responses. Together, the data suggest that amino-acid-dependent modulation of mitochondrial dynamics reflects increased Mfn1- and Opa1-dependent fusion rather than an inhibition of fission.

MTORC1- and PKA-independent sensing of amino acids

We previously investigated the ability of QLR addback to inhibit autophagy via re-activation of MTORC1 (Nwadike et al., 2018). To determine if MTORC1 was involved in sensing QLR upstream of mitochondrial fusion, we used the ATP competitive inhibitor Torin1 (Thoreen et al., 2009). We first confirmed that QLR supplementation to starvation medium re-activated MTORC1 (in 4T1 and U2OS cells) via phosphorylation of substrate ULK1 at serine 757 and downstream target of the MTORC1/S6 kinase axis, ribosomal protein S6 at serines 240/244 (Figures 2A, 2B, and S2A). Importantly, these effects were attenuated by Torin1. As we investigated mitochondrial sizes, we found that MTORC1 inhibition using Torin1 was not sufficient to promote a fusion response (under full-nutrient conditions) (Figure 2C). Torin1 also showed only a mild inhibitory effect on mitochondrial hyperfusion after QLR addback. These findings suggest that amino acid starvation and QLR addback both signal to mitochondrial fusion via MTORC1-independent routes.

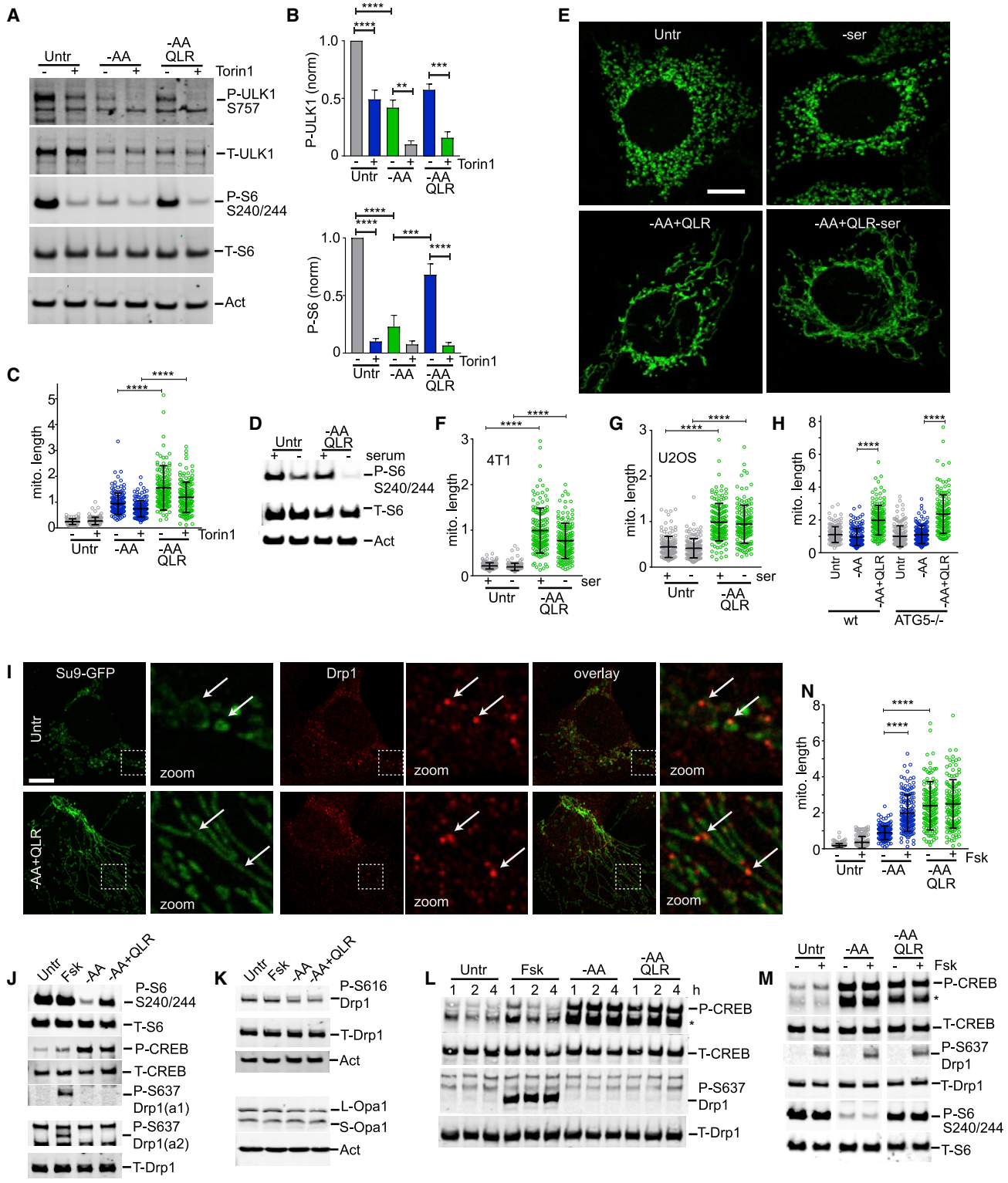

Figure 2. QLR control of mitochondrial hyperfusion is MTORC1 and PKA independent

(A) 4T1 cells were fully starved of amino acids (−AA) or incubated in EBSS starvation medium supplemented with QLR ± Torin1 (0.25μM) for 4 h. Protein phosphorylation status was assessed as indicated.

(B) Quantification of phosphorylation signals from (A) normalized to actin plotted as arbitrary units relative to untreated cells. N = 3 biological replicates, mean ± SEM shown.

(legend continued on next page)

MTORC1 activation by amino acids is also dependent on interaction with Rheb at the lysosome (Sancak et al., 2007, 2010), which is promoted by growth factor regulation of the TSC complex. As follows, we first confirmed that QLR-dependent re-activation of MTORC1 strictly requires growth factors (provided from serum) (Figure 2D). In 4T1/Su9GFP cells, mitochondria remained small sized upon serum withdrawal (Figures 2E and 2F). Mitochondrial hyperfusion was also induced by QLR addback regardless of serum availability. Similar trends were observed in U2OS/Su9GFP cells (Figure 2G). Taken together, these data suggest that the induction of amino-acid-dependent mitochondrial hyperfusion is independent of MTORC1.

Amino-acid-dependent fusion was proposed to allow mitochondria to evade degradation in autophagosomes and sustain bioenergetics. To further explore metabolic pathways potentially controlling mitochondrial fusion, we addressed the role of autophagy. ATG5 KO MEFs that are unable to induce autophagosome formation were tested (Gallagher et al., 2017; Kuma et al., 2004). Similar to wild-type, ATG5 KO MEFs produced hyperfused mitochondria in response to Q, L, and R addback relative to cells challenged with full amino acid starvation (Figures 2H and S2B). These findings suggest that mitochondrial hyperfusion from QLR supplementation is independent from autophagy.

Mitochondrial evasion of autophagy involved phosphorylation of Drp1 serine 637 (Gomes et al., 2011a), which disrupts mitochondrial recruitment to shift the balance toward fusion (Chang and Blackstone, 2007). As such, localization of Drp1 following starvation and QLR supplementation was assessed to determine if altered Drp1 distribution could explain hyperfusion. In resting U2OS/Su9GFP cells, Drp1 could be detected as fine punctate structures that co-localized on mitochondria (Figure 2I). Interestingly, Drp1 localization on mitochondria remained constant, even upon increased fusion driven by QLR addback. These results suggest that QLR-dependent hyperfusion was not due to Drp1 post-translational modification.

To further clarify, we investigated involvement of PKA, which phosphorylates Drp1-S637 to promote mitochondrial fusion (Chang and Blackstone, 2007; Gomes et al., 2011a, b). As control, we compared with PKA stimulation via forskolin (Fsk) and monitored the established PKA readout, CREB phosphorylation (Gonzalez and Montminy, 1989; Harada et al., 1999) (Figure 2J). As expected, Fsk treatment led to increased phosphorylation of both CREB-S133 and Drp1-S637 relative to untreated cells. However, amino acid starvation led to stronger CREB phosphorylation, and these levels remained high even upon QLR supplementation. Surprisingly, PKA activation via amino acid starvation did not promote Drp1-S637 phosphorylation and, furthermore, QLR supplementation did not show detectable effects. As this was unexpected, trends were confirmed with a second phospho-Drp1-S637 antibody. QLR-dependent re-activation of MTORC1 was confirmed in these samples. Since QLR-dependent hyperfusion did not involve Drp1-S637, we further investigated Drp1 phospho-site S616, which is a reported target of CDK1, PKC, and ERK2 that promotes mitochondrial fission (Kashatus et al., 2015; Qi et al., 2011; Serasinghe et al., 2015; Taguchi et al., 2007). Phosphorylation of Drp1 at S616 did not dramatically change under our different treatments (Figure 2K). Therefore, decreased phosphorylation of Drp1 S616 does not appear to drive Fsk- or QLR-dependent mitochondrial hyperfusion.

Mitochondrial dynamics can also be altered via Opa1-proteolytic processing. The long (L)-Opa1 form is associated with fusion while processing to short (S)-Opa1 enhances mitochondrial fragmentation (Duvezin-Caubet et al., 2006; Head et al., 2009; Ishihara et al., 2006). We observed that Opa1 was present in both L-Opa1 and S-Opa1 forms at unchanging ratios in all treatments (Figure 2K). As such, Opa1 remodeling does not underlie QLR-dependent mitochondrial hyperfusion.

Our data above suggested existence of distinct signaling pathways downstream of PKA. To re-examine the unexpected lack of "pro-fusion" activation at Drp1-S637 by amino acids, we considered that phosphorylation might be early and transient. Fsk activated Drp1-S637 phosphorylation within 1 h of treatment and remained sustained (Figure 2L), while CREB only showed modest phosphorylation. In contrast, amino acid starvation led to strong CREB phosphorylation within 1 h and also remained sustained, although Drp1-S637 was unresponsive. Furthermore, QLR supplementation did not modulate starvation-induced CREB phosphorylation. We further clarified whether Drp1-S637 phosphorylation was involved in QLR-mediated hyperfusion. 4T1/Su9GFP cells stimulated with Fsk (under full-nutrient conditions) showed only relatively modest levels of mitochondrial fusion, despite overt phosphorylation at Drp1-S637 (Figures 2M

(C) 4T1/Su9GFP cells treated for 4 h as in (A) were analyzed for mitochondrial length (arbitrary units relative to amino acid starvation as 1). Quantification of N = 150 cells; three experiments.
(D–F) 4T1/Su9GFP cells were incubated in EBSS starvation medium supplemented with QLR ± 10% dialyzed FBS. Quantification of N = 150 cells; three experiments (relative to QLR addback/dialyzed FBS as 1).
(G) Experiment in (F) carried out in U2OS/Su9GFP cells. N = 150 cells; three experiments.
(H) wt or ATG5 (−/−) MEFs were starved as indicated for 4 h and assayed for mitochondrial fusion (relative to amino acid starvation of wt as 1). N = 150 cells; three experiments.
(I) U2OS/Su9GFP cells were incubated in starvation medium supplemented with QLR for 4 h. Cells were immunostained for Drp1. Zoomed inset: arrow indicates localization of Drp1 (+) puncta on normal and hyperfused mitochondria.
(J and K) 4T1 cells were treated with forskolin (Fsk, 20 μM), amino acid starvation, or starvation/QLR supplementation for 4 h, and cell lysates were analyzed by immunoblot. Two different antibodies for phospho-S637-Drp1 were compared.
(L) 4T1 cells were treated as indicated for 1–4 h and analyzed by immunoblot. Asterisk (*) indicates non-specific P-CREB band that does not overlay with total CREB (confirmed via two-channel blot imaging).
(M and N) 4T1/Su9GFP cells were incubated under indicated starvation conditions ± forskolin (20 μM) for 4 h and analyzed for mitochondrial fusion or protein phosphorylation. N = 150 cells; three experiments (relative to −AA as 1). Statistical comparisons were analyzed by one-way ANOVA with Bonferroni post tests as indicated. **$p < 0.01$, ***$p < 0.001$, ****$p < 0.0001$. All mitochondrial quantification show mean ± SD. All starvation medium conditions contained 10% dialyzed FBS (except as indicated in D–G). All scale bars: 10 μm.

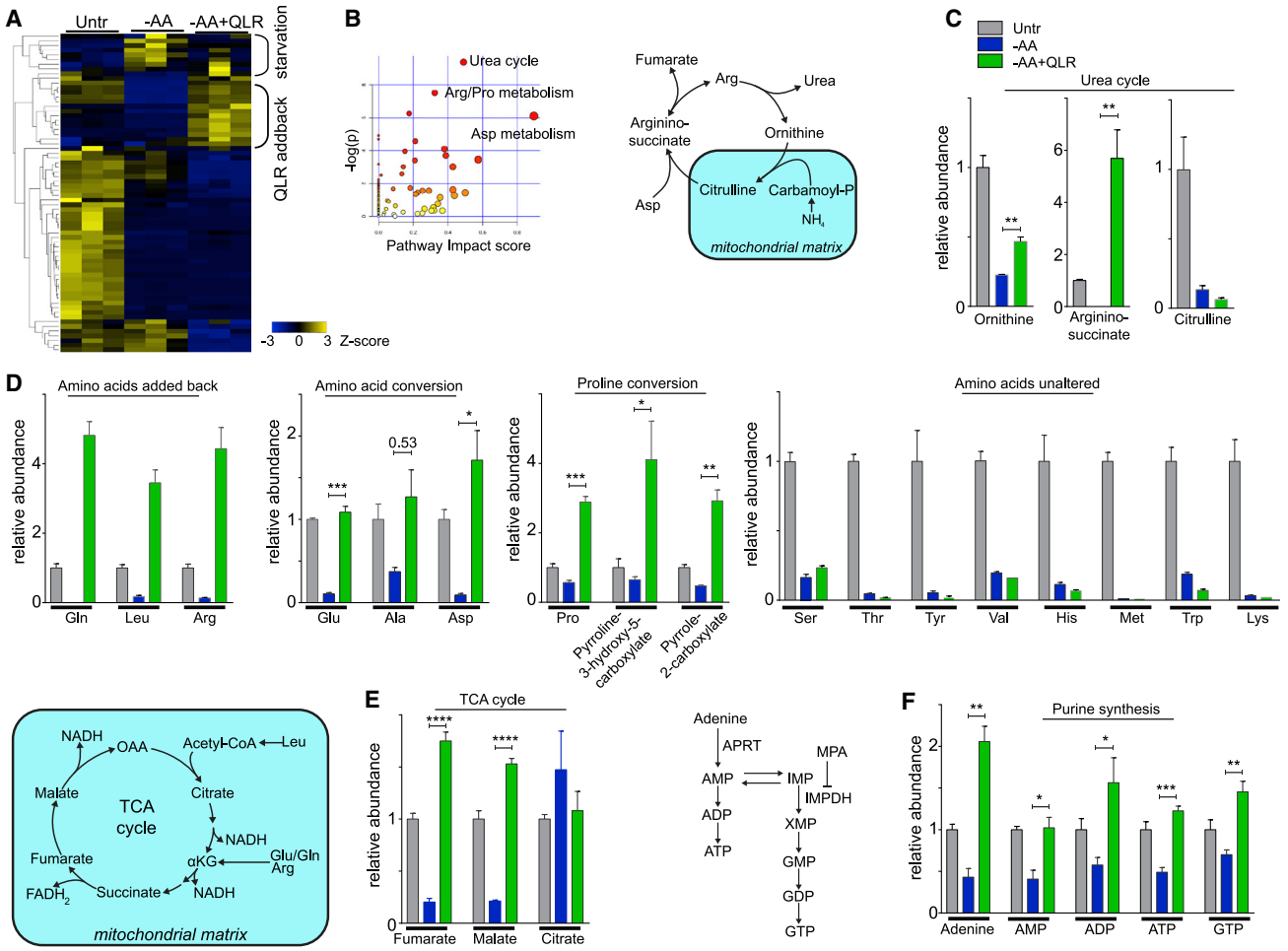

Figure 3. QLR supplementation leads to metabolic reprogramming of amino acid and nucleotide pathways

(A) 4T1 cells were incubated under amino acid starvation (−AA) or in starvation medium supplemented with QLR for 4 h. Starvation conditions contained 10% dialyzed FBS. Extracts were analyzed by liquid chromatography-mass spectrometry (LC-MS). Heatmap representation of amino acid pathways. N = 3 replicates per condition, representative of two independent experiments.

(B) Pathway analysis highlighting altered groups when comparing −AA versus −AA + QLR addback.

(C–F) Metabolite levels from (A) (arbitrary units relative to untreated condition) for key features of (C) urea cycle; (D) amino acid; (E) TCA cycle; and (F) purine biosynthesis pathways. N = 3. Average ± SEM shown. Statistical comparisons were analyzed as indicated by unpaired t tests. *p < 0.05, **p < 0.01, ***p < 0.001, ****p < 0.0001.

and 2N). Amino acid starvation promoted mitochondrial fusion, but without phosphorylation at Drp1-S637. However, Fsk treatment in combination with amino acid starvation led to strong levels of hyperfusion accompanied by phospho-Drp1-S637 accumulation. QLR addback in the context of amino acid starvation also led to strong hyperfusion, which appeared to be maximal as further Fsk treatment did not stimulate further fusion despite increased Drp1-S637 phosphorylation. Altogether, these results suggest multiple mechanisms controlling mitochondrial fusion. To this end, amino acid starvation may prime the system for further hyperfusion regulation via either Drp1-S637 phosphorylation or an independent QLR-sensing mechanism.

Metabolic reprogramming following amino acid addback

Results suggested an amino acid sensing pathway that coordinates mitochondrial dynamics independently of MTORC1. Exogenous amino acids, such as Q, L, and R, once transported into the cell, are metabolized to form a range of downstream derivatives (Lane and Fan, 2015; Spinelli et al., 2017). As such, we profiled metabolites in 4T1 cells after 4 h of amino acid starvation or QLR addback. Principal component analysis (Ivosev et al., 2008; Kirwan et al., 2012) showed clear clustering and distinct separation between treatment groups (Figure S3A). Overrepresentation and pathway impact analysis (Chagoyen and Pazos, 2013; Xia and Wishart, 2010, 2011) highlighted that QLR addback most prominently altered the urea cycle and, understandably, amino acid intermediates (Table S1). Cluster analysis (Figure 3A) highlighted metabolites that change upon full amino acid starvation and a further subset that is replenished upon QLR supplementation.

The urea cycle was one of the most affected pathways. In the urea cycle, cytosolic R is converted to ornithine, which gets

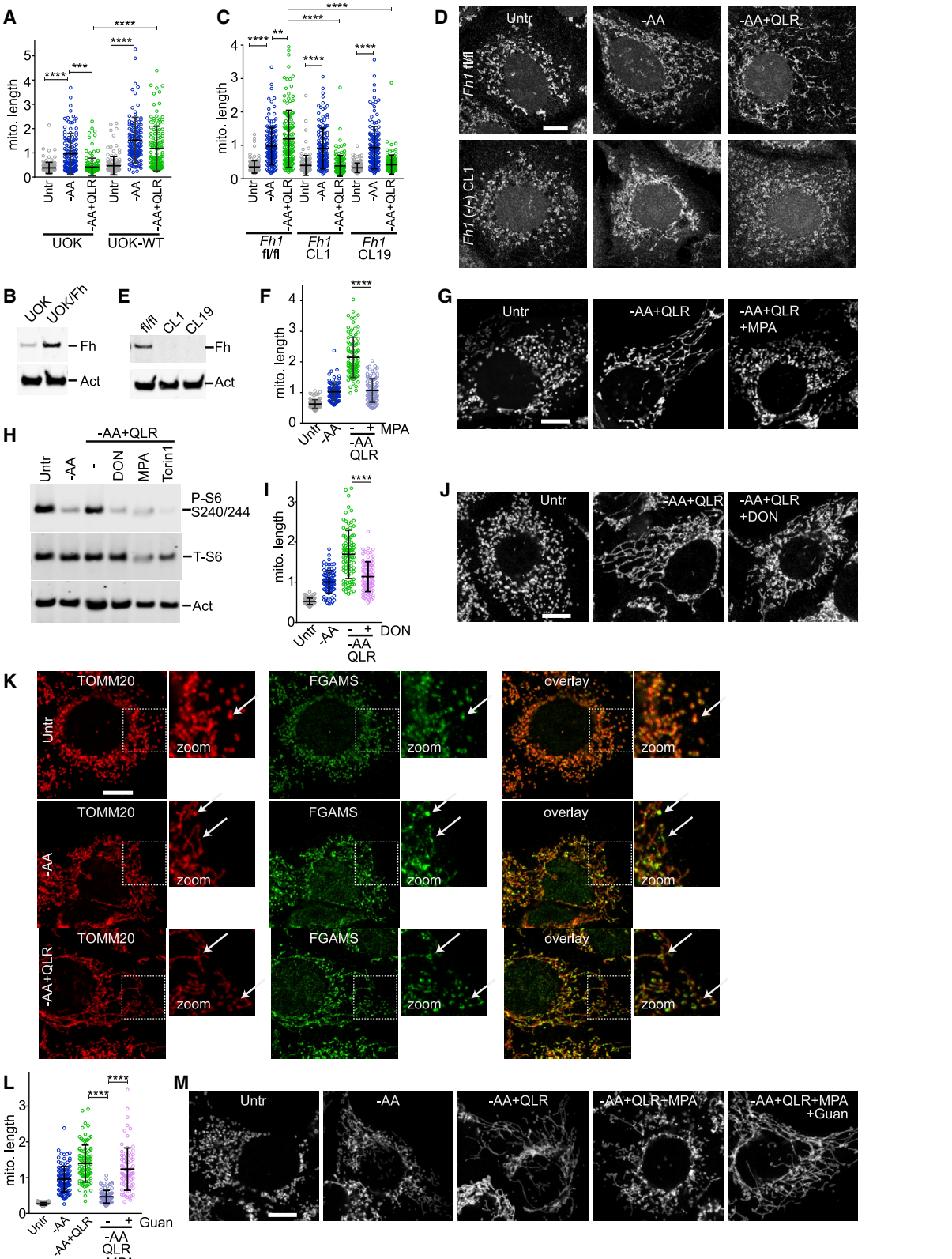

(legend on next page)

imported into mitochondria for conversion to citrulline (Keshet et al., 2018). Citrulline, exported back to the cytosol, gets converted to argininosuccinate, which is processed to form R. QLR supplementation leads to replenishment of ornithine and accumulation of argininosuccinate, but not the intermediate citrulline (Figure 3C). We were also interested in amino acid reprogramming. As follows, QLR supplementation replenished levels of central intermediate glutamate and other amino acids formed from glutamate, including alanine and aspartate (Figure 3D). Glutamate can also be converted to proline and we could detect this interconversion as well as intermediates within this pathway (Figures 3D and S3C) upon QLR supplementation. However, many other amino acid levels were not replenished by QLR addback (Figure 3D). Catabolism of QLR can also generate intermediates that re-feed the tricarboxylic acid (TCA) cycle, and indeed we detected replenishment of fumarate and malate (but not citrate) upon QLR addback (Figure 3E). Also, purine metabolism was identified by overrepresentation analysis and we confirmed that QLR supplementation led to accumulation of several purine intermediates including adenine, AMP, ADP, ATP, and GTP (Figure 3F). These data suggest that QLR supplementation to starved cells led to metabolic reprogramming, including pronounced amino acid catabolism and urea cycle flux. QLR addback leads to interconversion to a select group of other amino acids and also replenishes intermediates of the TCA cycle. Last, QLR bolsters purine biosynthesis.

Requirement of TCA cycle and purine biosynthetic pathways for hyperfusion

Fumarate and malate levels were responsive to QLR addback, consistent with reported roles for anaplerotic metabolites during amino acid sensing (Baracco et al., 2019; Duran et al., 2012; Son et al., 2019). To explore if these metabolites were involved during mitochondrial hyperfusion, we studied cells with loss of function in fumarate hydratase (Fh), which catalyzes hydration of fumarate to generate malate. Deficiency of Fh underlies the pathogenesis of hereditary leiomyomatosis renal cell carcinoma (HLRCC) (Tomlinson et al., 2002). Therefore, we investigated UOK262 Fh (−/−) HLRCC tumor-derived cells (Yang et al., 2010). We found that UOK262 cells contained a population of smaller, fragmented mitochondria (Figures 4A and 4B). Amino acid starvation on UOK262 led to mitochondrial fusion. However, QLR addback to amino acid starvation media reversed this. As control, we found that UOK262-WT cells (reconstituted with wild-type Fh) also showed starvation-dependent mitochondrial fusion. Strikingly, restoration of Fh activity rescued QLR-dependent hyperfusion.

To further clarify, we investigated immortalized kidney cells derived from mice with conditionally targeted Fh1 (Frezza et al., 2011). We confirmed in control (wild-type) Fh1 fl/fl cells that mitochondria in the basal resting state were overall of small sizes, mitochondrial fusion occurred upon amino acid starvation, and hyperfusion was promoted with QLR addback (Figures 6C–6E). Fh1 (−/−) cells showed normal basal and amino acid starvation mitochondrial fusion profiles. However, in both cell clones tested, Fh1 deletion blocked QLR-induced hyperfusion. These findings suggest that Fh activity is required for QLR-dependent mitochondrial hyperfusion.

Metabolism of QLR appeared critical for mitochondrial fusion. We noted above that QLR addback is paralleled by elevated levels of GTP. Since GTP binding can drive dimerization of Mfn1 upstream of fusion (Cao et al., 2017; Yan et al., 2018), we wondered if changes in GTP levels may play a causal role. QLR addback led to accumulation of adenine, AMP, ADP, ATP, and GTP (Figure 3F). This pattern suggested QLR-mediated IMP generation, which can be further converted to GTP in part via the activity of inosine-5′-monophosphate dehydrogenase (IMPDH). IMPDH function at this rate-limiting step is an attractive drug target (Huang et al., 2018; Liao et al., 2017). Interestingly, mitochondrial fusion driven by QLR addback was fully blocked by addition of the IMPDH inhibitor mycophenolic acid (MPA) (Figures 4F and 4G). Therefore, QLR-mediated mitochondrial hyperfusion appears dependent upon purine biosynthesis.

These results further suggested metabolic links between QLR supplementation and mitochondrial hyperfusion. Since glutaminolysis can activate MTORC1 (Duran et al., 2012), we first confirmed that treatment of 4T1 cells with the glutaminase inhibitor L-DON prevented QLR-mediated phosphorylation of S6 (Figure 4H). MPA was also found to inhibit MTORC1, consistent with previous reports on purine sensing (Emmanuel et al., 2017; Hoxhaj et al., 2017). Importantly, L-DON also inhibited mitochondrial hyperfusion following QLR supplementation (Figures 4I and 4J), consistent with a requirement for glutaminolysis in this mitochondrial remodeling response.

To further explore pathways underpinning QLR-mediated hyperfusion, we questioned whether the purinosome complex, which drives *de novo* synthesis of IMP, was involved (Pedley and Benkovic, 2017). The mammalian purinosome complex

Figure 4. QLR-dependent mitochondrial hyperfusion depends on fumarate hydratase and purine biogenesis via IMPDH

(A and B) UOK262 Fh-deficient or UOK262 cells reconstituted with wild-type Fh (UOK-WT) were incubated as indicated for 4 h and measured for mitochondrial hyperfusion after TOMM20 staining. N = 150 cells; three experiments. Control immunoblots for Fh expression shown.

(C–E) *Fh1*(fl/fl) control, clone1(−/−) and clone19(−/−) cells were tested as in (A). N = 150 cells; three experiments. Control immunoblots for Fh shown.

(F and G) 4T1/Su9GFP cells were incubated under starvation or QLR addback conditions ± MPA (1 μM) as indicated. N = 90 cells; three experiments.

(H) 4T1 cells were incubated under indicated starvation conditions ± L-DON (10 μM), MPA (1 μM), or Torin1 (0.25 μM) for 4 h and analyzed for S6 phosphorylation.

(I and J) 4T1 cells were incubated under starvation or QLR addback conditions ± L-DON (10 μM) as indicated for 4 h and measured for mitochondrial hyperfusion after TOMM20 staining. N = 90 cells; three experiments.

(K) 4T1 cells were pre-conditioned in purine-free culture medium. Cells were then treated as indicated for 4 h. Cells were stained for TOMM20 and FGAMS. Zoomed inset: arrows highlight examples of colocalization.

(L and M) 4T1 cells were incubated under starvation or QLR addback conditions (± MPA, 1 μM, ± guanosine, 20 μM) for 4 h and measured for mitochondrial hyperfusion after TOMM20 staining. N = 90 cells; three experiments. Statistical comparisons were analyzed as indicated by one-way ANOVA, Bonferroni post test. **p < 0.01, ***p < 0.001, ****p < 0.0001. All mitochondrial size quantifications show mean ± SD. All quantification relative to –AA in control cells as 1 and all starvation conditions contained 10% dialyzed FBS. Scale bars: 10 μm.

contains at least six core enzymes, including phosphoribosyl formylglycinamidine synthase (FGAMS), which catalyzes the fourth step of the purine biosynthetic sequence. Localization of the purinosome complex onto mitochondria-associated populations has been followed using FGAMS as a marker (French et al., 2013, 2016). In 4T1 cells (pre-conditioned in purine-free medium), we found that endogenous FGAMS was detected in distinct puncta that co-localized with TOMM20 on mitochondria (e.g., in basal resting conditions) (Figure 4K). FGAMS(+) purinosomes remained strongly associated on mitochondria following subsequent amino acid-starvation or QLR-supplementation conditions. We also observed robust association of FGAMS on mitochondria following QLR supplementation using 4T1 cells without purine-free pre-conditioning (Figure S4). Therefore, the purinosome complex remains associated on mitochondria under a range of nutrient contexts to provide a potential mechanism for localized purine generation following QLR supplementation.

We observed that IMPDH inhibition suppressed QLR-dependent mitochondrial hyperfusion by preventing conversion of IMP to GMP (and ultimately GTP). In addition to *de novo* synthesis, GMP can also be generated via purine salvage pathways. Using these routes, supplementation of guanosine to the cell culture medium has been shown to replenish cellular guanine and resulting GTP levels (Ji et al., 2006). Consistent with this, we found that supplementation with guanosine was able to rescue QLR-mediated mitochondrial hyperfusion that was inhibited via MPA (Figures 4L and 4M). These findings further suggest that GTP production is a key driver of mitochondrial fusion.

Q supplementation replenishes anaplerotic and nucleotide biosynthetic pathways

We propose that supplemented QLR amino acids are metabolized toward purine biosynthesis to trigger mitochondrial fusion. We performed stable isotope tracer analysis to further clarify the QLR contribution to metabolic pathways. Since Fh and the TCA cycle were critically required for hyperfusion, we first tested 4T1 cells in amino acid-starvation conditions supplemented with [$^{13}C_5$]-Q (combined with L + R). We confirmed that [$^{13}C_5$]-Q was rapidly deaminated to form glutamate within 15 min of supplementation (Figures 5A and 5B). Reassuringly, we detected entry of ^{13}C-labeled Q carbons into the TCA cycle, as illustrated by formation of m+5 α-ketoglutarate and m+4 malate isotopomers. Interestingly, incorporation of [$^{13}C_5$]-Q into TCA intermediates and glutathione was not overly affected by MTOR inhibition (Figures S5A and S5B). Next, potential utilization of Q for nucleotide synthesis was explored. Notwithstanding that we observed [$^{13}C_5$]-Q derived carbons entering pyrimidine biosynthetic pathways (e.g., for UDP, TDP) (Figures S5C and S5D), QLR supplementation did not lead to replenishment of pyrimidine levels (Figure S5E). As expected, labeling from [$^{13}C_5$]-Q did not channel into purine biosynthesis (Figure S5D).

Metabolism of Q via glutaminolysis helps provide nitrogen groups for nucleotide biosynthesis (Kurmi and Haigis, 2020). Therefore, we traced doubly labeled [$^{15}N_2$]-Q in the context of QLR supplementation. During *de novo* purine biosynthesis, Q contributes at multiple stages via transfer of the amide nitrogen and donation of the amine nitrogen through carriers: glycine and aspartate (Pedley and Benkovic, 2017) (Figures 5C, full map in S6). Fitting this scheme, supplementation of starvation conditions with [$^{15}N_2$]-Q (+L+R) led to labeling of IMP within 15 min (Figure 5D). IMP displayed a complex range of isotopologues, with m+4 isotopomers appearing within 2 h of incubation. Furthermore, m+5 labeling of GMP and AMP (formed downstream of IMP) was also detected within 2 h (Figure 5D). Therefore, supplemented Q readily contributes to purine biosynthesis by donating amine groups, consistent with our model for hyperfusion regulation.

Amino-acid-dependent hyperfusion is distinct from SIMH

We next investigated the potential relationship between amino-acid-dependent mitochondrial fusion and the SIMH response associated with disrupted ER proteostasis (Lebeau et al., 2018; Tondera et al., 2009). Protein synthesis inhibitor cycloheximide (CHX) was used to induce SIMH in combination with amino acid starvation and QLR supplementation (Figures 6A and 6B). Mitochondrial hyperfusion was indeed observed in CHX-treated cells (under full-nutrient conditions). Interestingly, CHX further increased mitochondrial length in amino-acid-starved cells. Last, while QLR addback (into amino acid starvation medium) led to clear mitochondrial hyperfusion, addition of CHX in this condition only had a small further stimulatory effect. Therefore, CHX- or QLR-induced hyperfusion may both represent near-maximal levels of mitochondrial remodeling. However, CHX appears to promote some mitochondrial fusion signals that were independent of QLR addback. To further clarify, we found that CHX still induced strong SIMH regardless of Fh ablation (Figure 6C). Hyperfusion stimulated by CHX was also not blocked by MPA (Figure 6D). In addition, although the PERK-ATF4 axis has been implicated in ER-stress-related SIMH (Lebeau et al., 2018), QLR supplementation did not alter ATF4 levels compared with amino-acid-starved cells (Figure S7), Therefore, SIMH has different molecular underpinnings than QLR-driven hyperfusion.

Since nutrient-sensitive hyperfusion and SIMH appeared distinct, we further explored potential interactions between nutrient-addback and stress response pathways. One quality control pathway that works in parallel with mitophagy is PINK1/parkin-dependent generation of mitochondria-derived vesicles (MDVs) (McLelland et al., 2014; Soubannier et al., 2012). In response to oxidative stress or defective autophagy, damaged mitochondrial content is selectively packaged into TOMM20(+) MDV, which then fuse to degradative lysosomes (McLelland et al., 2016; Towers et al., 2021). Resting 4T1 cells did not generate MDV from their basal mitochondria (Figure 6E). In contrast, upon CHX treatment, prominent TOMM20(+) vesicles budded off hyperfused mitochondria. The TOMM20(+) signal did not co-localize with general mitochondrial content marked by Su9-GFP, consistent with selective cargo formation (Neuspiel et al., 2008; Soubannier et al., 2012). In addition, amino acid starvation promoted MDV formation from elongated mitochondria. Interestingly, MDV formation was still detected from hyperfused mitochondria following QLR addback. MDV formation following protein synthesis inhibition would be expected. However, MDVs indicate levels of mitochondrial stress following

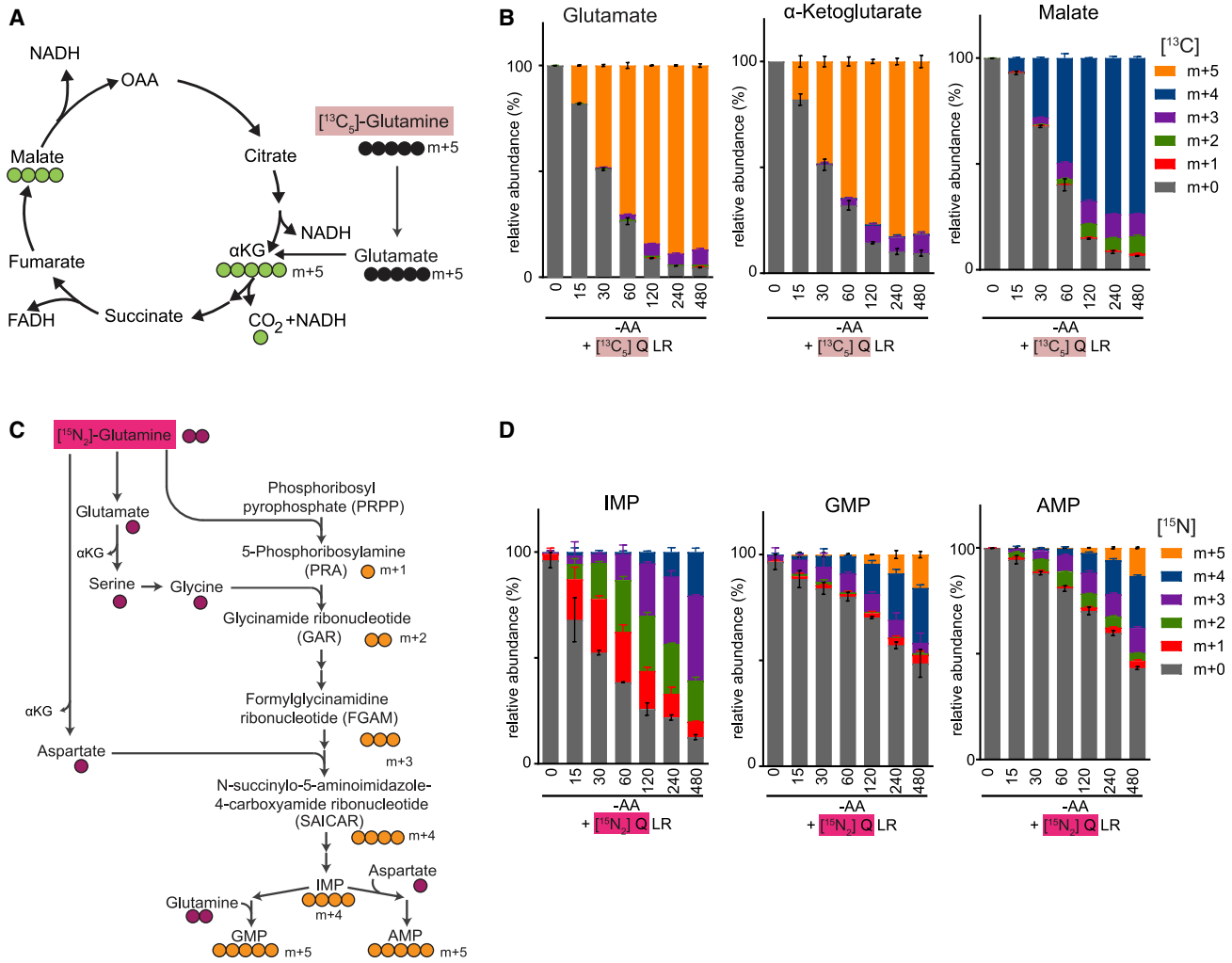

Figure 5. Q-derived carbon and nitrogen replenish distinct metabolic pathways

(A) Stable isotope tracing into TCA cycle intermediates using [$^{13}C_5$]-Q.

(B) 4T1 cells were incubated in amino acid starvation + QLR supplementation (containing [$^{13}C_5$]-Q) for 0 to 480 min (i.e., 8 h).

(C) Stable isotope tracing into the purine biosynthetic pathway using [$^{15}N_2$]-Q.

(D) 4T1 cells were incubated in amino acid starvation + QLR supplementation (containing [$^{15}N_2$]-Q) for 0 to 480 min. Levels of metabolites and isotope incorporation were determined by LC-quadrupole time of flight (QTOF). Data represent N = 3 replicates per condition, average ± SD shown. All starvation conditions contained 10% dialyzed FBS.

amino acid starvation that still exist during QLR-supplementation conditions. Therefore, QLR-induced mitochondrial hyperfusion appears distinct from the MDV mitochondrial homeostasis pathway.

We wished to gain further insight into physiological roles of QLR-dependent mitochondrial hyperfusion. Since mitochondrial dynamics can regulate entry into apoptosis (Cipolat et al., 2006; Frank et al., 2001; Frezza et al., 2006; Wasiak et al., 2007) and SIMH has been shown to suppress apoptosis (Tondera et al., 2009), we explored roles for QLR-dependent mitochondrial hyperfusion in cell survival. We found that short exposure to staurosporine induces cleavage of caspase 3, detected as distinct cytosolic puncta (as previously reported) (Villar et al., 2017) (Figure 7A). Puncta were juxtaposed to mitochondria consistent with cytochrome *c* release followed by localized apoptosome formation and caspase 3 activation. From puncta quantification, we found that 4-h treatment of CHX alone did not activate caspase 3 (Figure 7B). Amino acid starvation led to mild caspase 3 activation, which was reversed by QLR addback. Interestingly, CHX treatment suppressed the ability of staurosporine to promote caspase 3 activation, consistent with an anti-apoptotic role for SIMH. In contrast, cells challenged with amino acid starvation were strongly sensitized to staurosporine and this was reversed by QLR addback. These results are consistent with an anti-apoptotic function for mitochondrial hyperfusion. To understand wider relationships with apoptosis, we studied MEFs with KO of genes required for mitochondrial fusion. Cells were examined following more prolonged (overnight) treatment with BH3-memetic ABT-737 to activate the mitochondrial Bcl-2/Bcl-XL apoptotic pathway.

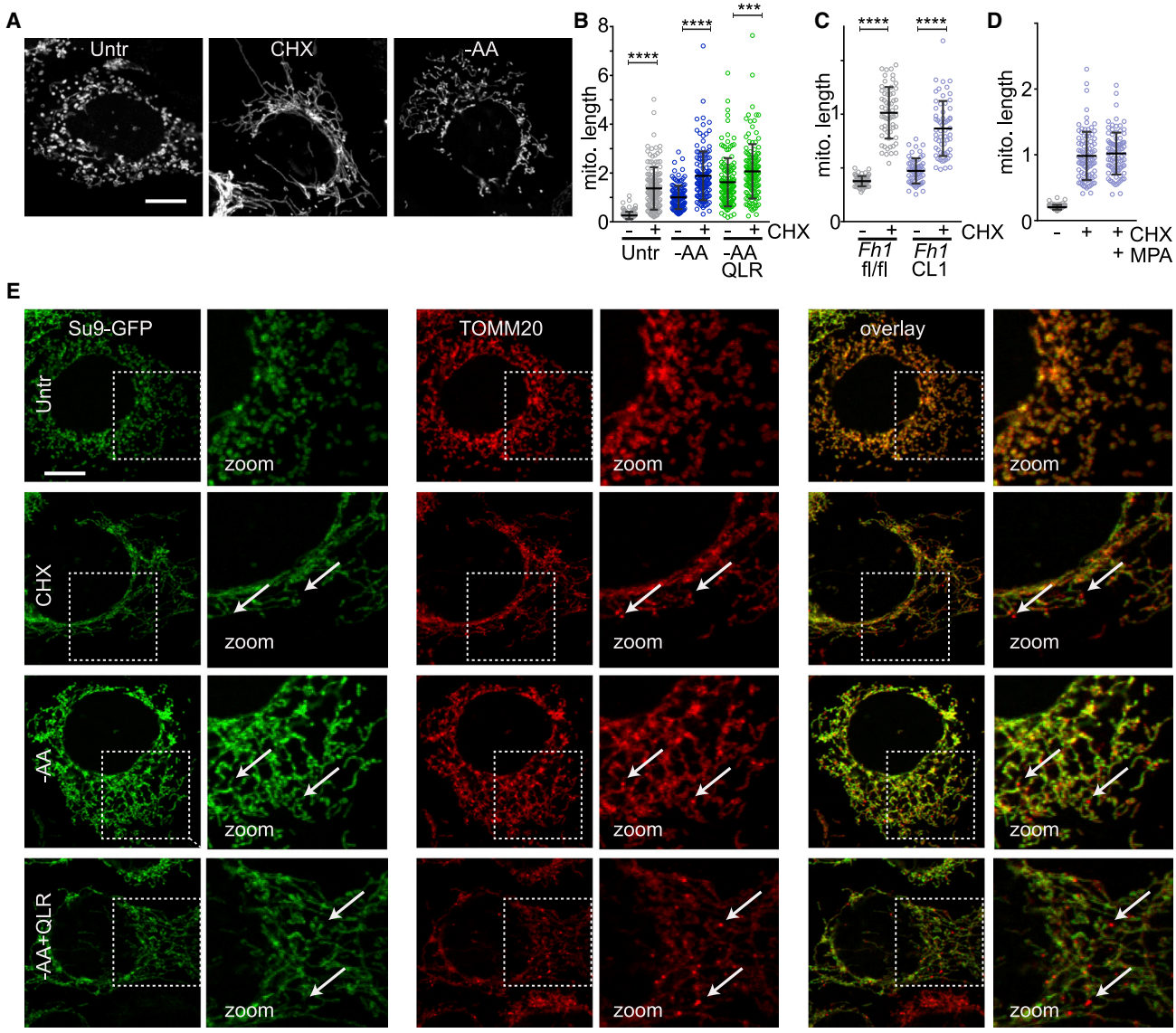

Figure 6. SIMH does not require Fh or IMPDH activities

(A) 4T1/Su9GFP cells were incubated with cycloheximide (CHX, 10 μM) (under full nutrients) or starved of amino acids for 4 h.

(B) Cells as in (A) were incubated in starvation or QLR addback ± CHX as indicated for 4 h. N = 150 cells; three experiments (relative to –AA as 1).

(C) *Fh1*(fl/fl) control or clone1(−/−) were incubated with CHX as indicated. N = 60 cells; two experiments (relative to CHX in fl/fl as 1).

(D) 4T1/Su9GFP cells were incubated with CHX ± MPA (1 μM) as indicated. N = 90 cells; three experiments (relative to –AA as 1).

(E) 4T1/Su9GFP cells were treated to CHX, starvation, or QLR-addback conditions for 4 h. Cells stained for TOMM20. Zoomed inset: arrows indicate MDV enriched for TOMM20. Statistical comparisons were analyzed as indicated by one-way ANOVA, Bonferroni post test. ***$p < 0.001$, ****$p < 0.0001$. All mitochondrial quantifications show mean ± SD. Starvation conditions contained 10% dialyzed FBS. Scale bars: 10 μm.

Wild-type MEF showed caspase 3 activation following ABT-737 treatment and this response was exaggerated in Mfn1 KO MEFs (Figure 7C). Prolonged nutrient (amino acid and serum) starvation or serum starvation alone also activated caspase 3 cleavage, but these responses were dampened by Mfn1 KO. Interestingly, Opa1 KO also showed differential roles for ABT-737 versus serum starvation-dependent apoptosis. To further clarify, we tested 4T1 cells following stable silencing of Opa1. Loss of Opa1 was confirmed to result in constitutively fragmented mitochondria that were non-responsive to starvation or QLR supplementation (Figures 7D–7F) (as observed in Opa1 KO MEFs). Furthermore, loss of Opa1 in 4T1 cells decreased apoptotic sensitivity toward prolonged serum starvation but caused hypersensitivity toward ABT-737 (Figures 7G and 7H). Therefore, mitochondrial fusion can play pro-apoptotic roles under serum-depletion stress conditions, but carry pro-survival roles to control intrinsic mitochondrial-dependent apoptotic pathways.

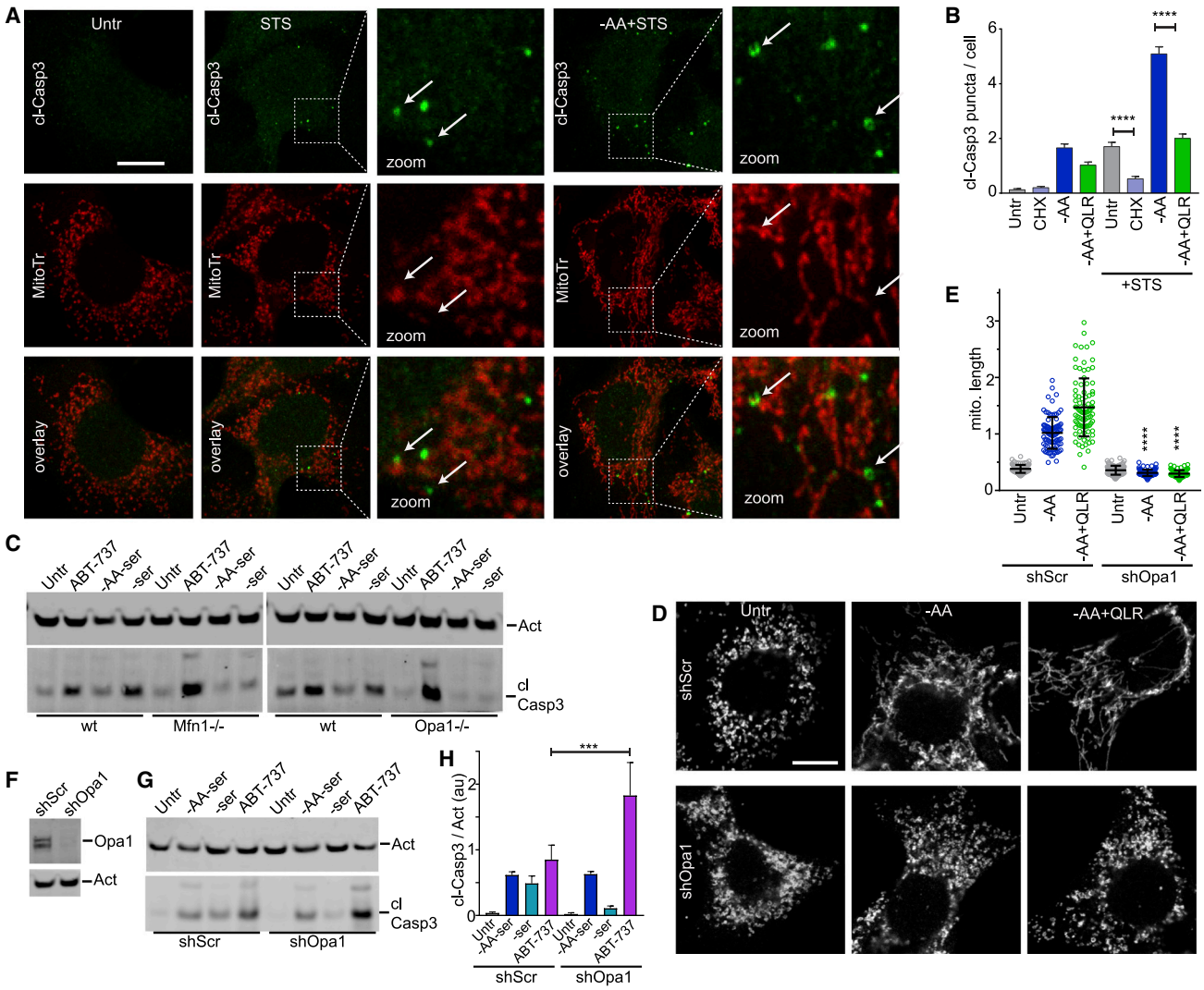

Figure 7. QLR-induced mitochondrial hyperfusion suppresses apoptosis

(A) 4T1 cells were treated to 1 h of staurosporin (STS, 1 μM) either in basal (full-nutrient) or amino acid starvation-conditions. Cells were stained with Mitotracker orange and antibodies for cleaved caspase 3. Zoomed inset: arrows indicate puncta of activated caspase 3 juxtaposed to mitochondria.

(B) Experiment in (A) quantified as activated caspase puncta/cell (average ± SEM). N = 90 cells; three experiments.

(C) Matched wt versus Mfn1 (−/−) MEF, or matched wt versus Opa1(−/−) MEF were incubated with ABT-737 (20 μM) or starved as indicated for 20 h. Cell lysates were assayed for caspase 3 cleavage. Representative of three experiments.

(D–F) 4T1 were derived that stably expressed shRNA for Opa1 (or scrambled shRNA control). Knockdown was confirmed by immunoblotting. Cells were incubated in starvation conditions as indicated for 4 h and measured for mitochondrial hyperfusion after TOMM20 staining. Mitochondrial size quantifications show mean ± SD. N = 90 cells; representative of three experiments.

(G and H) 4T1 stably expressing shRNA for Opa1 (or scrambled control) were incubated with ABT-737 (20 μM), or starved as indicated for 18 h. Cell lysates were assayed for caspase 3 cleavage, with quantification (average ± SEM). N = 3 replicates. Starvation conditions contained 10% dialyzed FBS (in A, B, D, E). Statistical comparisons were analyzed by one-way ANOVA, Bonferroni post test (in E, comparing starvation condition in shOpa1 versus equivalent condition in sh scrambled control), or as indicated by unpaired t tests (in B and H). ***p < 0.001, ****p < 0.0001. Scale bars: 10 μm.

DISCUSSION

Here, we identify a hitherto unappreciated pathway linking amino acid cues to the regulation of mitochondrial fusion. In agreement with previously proposed models (Gomes et al., 2011a; Rambold et al., 2011b), amino acid starvation robustly promotes mitochondrial fusion. To decipher the signals that controlled mitochondrial fusion, we re-supplemented Q, L, and R into starvation medium, as we previously characterized how QLR addback was able to negatively regulate autophagy (Nwadike et al., 2018). Surprisingly, QLR addback led to strong mitochondrial hyperfusion, opposite to predictions. We have not yet tested all possible combinations of amino acid addback but so far have found QLR to promote the highest levels of mitochondrial hyperfusion. Interestingly, addback of Q + L (under amino acid-starvation conditions) has also been proposed to cause

unbalanced glutaminolysis and MTORC1 activation (Duran et al., 2012), which, when left for prolonged time frames, activates apoptosis (Villar et al., 2017).

Although MTORC1 has been shown to regulate mitochondrial biogenesis and dynamics (Morita et al., 2017), QLR-dependent hyperfusion could be effectively uncoupled from MTORC1 signaling. The ability of QLR addback to induce mitochondrial hyperfusion was fully dependent on inner mitochondrial membrane fusion directed by Opa1, and, interestingly, also on Mfn1 function. Multiple lines of evidence also suggested that QLR-induced hyperfusion was independent from regulation of the mitochondrial fission factor, Drp1. So far, we conclude that QLR addback can stimulate hyperfusion via a mechanism that worked in parallel with Drp1-dependent modulation. Further metabolic profiling highlighted that QLR was readily incorporated into catabolic pathways, including incorporation of amino acid carbon backbones into the TCA cycle. Accordingly, a block of TCA cycle flux via Fh deficiency prevented QLR-dependent hyperfusion. We noticed that QLR addback replenished nucleotide intermediates, including GTP and other purine-related metabolites. This was intriguing since GTP binding to Mfn1 was shown to induce protein dimerization, resulting in outer mitochondrial membrane fusion (Cao et al., 2017; Qi et al., 2016). Following supplementation of QLR, IMP appeared to be replenished, which can be further transformed into GMP via IMPDH, leading to formation of GTP. Interestingly, inhibition of IMPDH activity strongly blocked QLR-dependent hyperfusion. These data suggest that QLR addback was generating elevated GTP levels that were sensed by Mfn1, leading to mitochondrial fusion. GTP has been shown to promote fusion of isolated mitochondria *in vitro* in an Mfn1-dependent manner (Hoppins et al., 2011; Pyakurel et al., 2015), and here we found that supplementation of guanosine was similarly able to promote mitochondrial hyperfusion. Furthermore, we used metabolic tracer studies to better clarify that carbon derived from Q replenished cellular pathways via the TCA cycle, while nitrogen derived from Q replenished purine biosynthetic pathways. Therefore, incorporation of both carbon and nitrogen from Q may be required to fully generate the nutrient-dependent signals for mitochondrial hyperfusion.

Here, we also explored whether nutrient-dependent hyperfusion was related to the previously characterized SIMH response. Both SIMH and amino acid starvation promoted formation of MDV, which may indicate increased levels of mitochondrial oxidative stress (Soubannier et al., 2012). However, MDV still formed during QLR addback, and SIMH following proteostasis disruption still occurred in cells lacking TCA cycle or IMPDH function. Therefore, QLR-dependent hyperfusion represents a distinct metabolically linked pathway for the regulation of mitochondrial dynamics. One function for SIMH is to decrease sensitivity toward apoptosis (Tondera et al., 2009), and a number of mechanisms link mitochondrial dynamics and cell death (Prudent et al., 2015). Indeed, QLR-dependent hyperfusion, like cycloheximide-induced SIMH, can reduce apoptosis levels.

Limitations of this study

In summary, we have characterised multiple pathways that control mitochondrial fusion, including a mechanism for MTORC1-independent sensing of the regulatory amino acids QLR. This mitochondria-based amino acid sensing links metabolic flux to the control of mitochondrial dynamics, thus establishing an additional pathway that functions independently of PKA-mediated regulation of Drp1 and proteostasis-dependent SIMH. It will be important to further understand if nutrient-dependent hyperfusion has roles in reciprocally modulating bioenergetic or metabolic functions of mitochondria. In addition, we need to determine how the nutrient-sensing mechanisms dissected here using model cell systems function within more physiological contexts.

STAR★METHODS

Detailed methods are provided in the online version of this paper and include the following:

- KEY RESOURCES TABLE
- RESOURCE AVAILABILITY
  - Lead contact
  - Materials availability
  - Data and code availability
- EXPERIMENTAL MODEL ANS SUBJECT DETAILS
  - Cell culture and treatments
- METHOD DETAILS
  - Immunoblot analysis
  - Microscopy
  - Steady state metabolite analysis
  - Stable isotope tracer analysis
  - Transmission electron microscopy
- QUANTIFICATION AND STATISTICAL ANALYSIS

SUPPLEMENTAL INFORMATION

Supplemental information can be found online at https://doi.org/10.1016/j.celrep.2022.111198.

ACKNOWLEDGMENTS

M.O.A. received support from the Lagos State Government Scholarship Board Nigeria. E.Y.W.C. is supported by the Cancer Research UK/West of Scotland Cancer Centre/Glasgow Cancer Centre, Tenovus Scotland, Natural Sciences and Engineering Research Council (NSERC) Canada (RGPIN-2018-05162), and Cancer Research Society/Société de Recherche sur le Cancer, Canada. R.X.Z. and C.L.M. received studentship support from Queen's University Department of Biomedical Sciences. D.P. is supported by a Canadian Institutes of Health Research (CIHR) Postdoctoral Fellowship (MFE-171312). E.-L.E. received support for this work from the University of Turku, Finland. I.T. is supported by a Fonds de recherche du Québec (FRQS) Senior Investigator award and the Terry Fox Foundation (TFF) Oncometabolism Team Grants TFF-242122 and TFF-116128. S.A.A. is supported by Cancer Research Society/Société de Recherche sur le Cancer (grant 25505) and CIHR (grants 394568 and 451069). Stable isotope tracer metabolic analysis was performed at The Rosalind and Morris Goodman Cancer Institute Metabolomics Innovation Resource, which is supported by the Canada Foundation for Innovation, The Dr. John R. and Clara M. Fraser Memorial Trust, the Terry Fox Foundation (TFF Oncometabolism Team Grant TFF-242122), and McGill University. The funders had no role in study design, data collection and interpretation, or the decision to submit the work for publication. We thank N. Mizushima (University of Tokyo) for ATG5KO MEFs and the Su9GFP expression construct, and David C. Chan (Caltech, Pasadena) for Opa1, Mfn1/2 single- and double-KO MEFs. We thank W. Marston Linehan for providing UOK262 cells systems and Christian Frezza (University of Cambridge) for providing Fh1 (fL/fL) and (−/−) cells.

NJWR and ZR acknowledge the Strathclyde Centre for Molecular Biosciences for support in analysis. We thank the Electron Microscopy Laboratory, Institute of Biomedicine, University of Turku, for technical help.

AUTHOR CONTRIBUTIONS

Conceptualization, M.O.A. and E.Y.W.C.; investigation, M.O.A., R.X.Z., C.L.M., D.P., C.M., K.B.P., C.C., D.B., M.A.-R., and N.F.A.-T.; writing – original draft, M.O.A. and E.Y.W.C.; supervision, E.Y.W.C., I.T., D.A., S.A.A., N.J.W.R., and D.G.W.; funding acquisition, E.Y.W.C., S.A.A., I.T., and E.-L.E.

DECLARATIONS OF INTERESTS

The authors declare no competing interests.

Received: November 6, 2020
Revised: June 6, 2022
Accepted: July 21, 2022
Published: August 16, 2022

REFERENCES

Anwar, T., Liu, X., Suntio, T., Marjamaki, A., Biazik, J., Chan, E.Y.W., Varjosalo, M., and Eskelinen, E.L. (2019). ER-targeted Beclin 1 supports autophagosome biogenesis in the absence of ULK1 and ULK2 kinases. Cells *8*, 475.

Babicki, S., Arndt, D., Marcu, A., Liang, Y., Grant, J.R., Maciejewski, A., and Wishart, D.S. (2016). Heatmapper: Web-enabled heat mapping for all. Nucleic Acids Res. *44*. W147–153.

Baracco, E.E., Castoldi, F., Durand, S., Enot, D.P., Tadic, J., Kainz, K., Madeo, F., Chery, A., Izzo, V., Maiuri, M.C., et al. (2019). alpha-Ketoglutarate inhibits autophagy. Aging *11*, 3418–3431.

Burman, J.L., Pickles, S., Wang, C., Sekine, S., Vargas, J.N.S., Zhang, Z., Youle, A.M., Nezich, C.L., Wu, X., Hammer, J.A., and Youle, R.J. (2017). Mitochondrial fission facilitates the selective mitophagy of protein aggregates. J. Cell Biol. *216*, 3231–3247.

Cao, Y.L., Meng, S., Chen, Y., Feng, J.X., Gu, D.D., Yu, B., Li, Y.J., Yang, J.Y., Liao, S., Chan, D.C., and Gao, S. (2017). MFN1 structures reveal nucleotide-triggered dimerization critical for mitochondrial fusion. Nature *542*, 372–376.

Carroll, B., Maetzel, D., Maddocks, O.D., Otten, G., Ratcliff, M., Smith, G.R., Dunlop, E.A., Passos, J.F., Davies, O.R., Jaenisch, R., et al. (2016). Control of TSC2-Rheb signaling axis by arginine regulates mTORC1 activity. Elife *5*, e11058.

Cereghetti, G.M., Stangherlin, A., Martins de Brito, O., Chang, C.R., Blackstone, C., Bernardi, P., and Scorrano, L. (2008). Dephosphorylation by calcineurin regulates translocation of Drp1 to mitochondria. Proc. Natl. Acad. Sci. USA *105*, 15803–15808.

Chagoyen, M., and Pazos, F. (2013). Tools for the functional interpretation of metabolomic experiments. Brief. Bioinform. *14*, 737–744.

Chambers, M.C., Maclean, B., Burke, R., Amodei, D., Ruderman, D.L., Neumann, S., Gatto, L., Fischer, B., Pratt, B., Egertson, J., et al. (2012). A cross-platform toolkit for mass spectrometry and proteomics. Nat. Biotechnol. *30*, 918–920.

Chang, C.R., and Blackstone, C. (2007). Cyclic AMP-dependent protein kinase phosphorylation of Drp1 regulates its GTPase activity and mitochondrial morphology. J. Biol. Chem. *282*, 21583–21587.

Chantranupong, L., Scaria, S.M., Saxton, R.A., Gygi, M.P., Shen, K., Wyant, G.A., Wang, T., Harper, J.W., Gygi, S.P., and Sabatini, D.M. (2016). The CASTOR proteins are arginine sensors for the mTORC1 pathway. Cell *165*, 153–164.

Chen, H., Detmer, S.A., Ewald, A.J., Griffin, E.E., Fraser, S.E., and Chan, D.C. (2003). Mitofusins Mfn1 and Mfn2 coordinately regulate mitochondrial fusion and are essential for embryonic development. J. Cell Biol. *160*, 189–200.

Chen, H., McCaffery, J.M., and Chan, D.C. (2007). Mitochondrial fusion protects against neurodegeneration in the cerebellum. Cell *130*, 548–562.

Chen, H., Vermulst, M., Wang, Y.E., Chomyn, A., Prolla, T.A., McCaffery, J.M., and Chan, D.C. (2010). Mitochondrial fusion is required for mtDNA stability in skeletal muscle and tolerance of mtDNA mutations. Cell *141*, 280–289.

Chen, Y., and Dorn, G.W., 2nd. (2013). PINK1-phosphorylated mitofusin 2 is a Parkin receptor for culling damaged mitochondria. Science *340*, 471–475.

Cipolat, S., Rudka, T., Hartmann, D., Costa, V., Serneels, L., Craessaerts, K., Metzger, K., Frezza, C., Annaert, W., D'Adamio, L., et al. (2006). Mitochondrial rhomboid PARL regulates cytochrome c release during apoptosis via OPA1-dependent cristae remodeling. Cell *126*, 163–175.

Creek, D.J., Jankevics, A., Burgess, K.E.V., Breitling, R., and Barrett, M.P. (2012). IDEOM: an Excel interface for analysis of LC-MS-based metabolomics data. Bioinformatics *28*, 1048–1049.

Cribbs, J.T., and Strack, S. (2007). Reversible phosphorylation of Drp1 by cyclic AMP-dependent protein kinase and calcineurin regulates mitochondrial fission and cell death. EMBO Rep. *8*, 939–944.

Durán, R.V., Oppliger, W., Robitaille, A.M., Heiserich, L., Skendaj, R., Gottlieb, E., and Hall, M.N. (2012). Glutaminolysis activates Rag-mTORC1 signaling. Mol. Cell *47*, 349–358.

Duvezin-Caubet, S., Jagasia, R., Wagener, J., Hofmann, S., Trifunovic, A., Hansson, A., Chomyn, A., Bauer, M.F., Attardi, G., Larsson, N.G., et al. (2006). Proteolytic processing of OPA1 links mitochondrial dysfunction to alterations in mitochondrial morphology. J. Biol. Chem. *281*, 37972–37979.

Dyall, S.D., Brown, M.T., and Johnson, P.J. (2004). Ancient invasions: from endosymbionts to organelles. Science *304*, 253–257.

Emmanuel, N., Ragunathan, S., Shan, Q., Wang, F., Giannakou, A., Huser, N., Jin, G., Myers, J., Abraham, R.T., and Unsal-Kacmaz, K. (2017). Purine nucleotide availability regulates mTORC1 activity through the Rheb GTPase. Cell Rep. *19*, 2665–2680.

Frank, S., Gaume, B., Bergmann-Leitner, E.S., Leitner, W.W., Robert, E.G., Catez, F., Smith, C.L., and Youle, R.J. (2001). The role of dynamin-related protein 1, a mediator of mitochondrial fission, in apoptosis. Dev. Cell *1*, 515–525.

French, J.B., Zhao, H., An, S., Niessen, S., Deng, Y., Cravatt, B.F., and Benkovic, S.J. (2013). Hsp70/Hsp90 chaperone machinery is involved in the assembly of the purinosome. Proc. Natl. Acad. Sci. USA *110*, 2528–2533.

French, J.B., Jones, S.A., Deng, H., Pedley, A.M., Kim, D., Chan, C.Y., Hu, H., Pugh, R.J., Zhao, H., Zhang, Y., et al. (2016). Spatial colocalization and functional link of purinosomes with mitochondria. Science *351*, 733–737.

Frezza, C., Cipolat, S., Martins de Brito, O., Micaroni, M., Beznoussenko, G.V., Rudka, T., Bartoli, D., Polishuck, R.S., Danial, N.N., De Strooper, B., and Scorrano, L. (2006). OPA1 controls apoptotic cristae remodeling independently from mitochondrial fusion. Cell *126*, 177–189.

Frezza, C., Zheng, L., Folger, O., Rajagopalan, K.N., MacKenzie, E.D., Jerby, L., Micaroni, M., Chaneton, B., Adam, J., Hedley, A., et al. (2011). Haem oxygenase is synthetically lethal with the tumour suppressor fumarate hydratase. Nature *477*, 225–228.

Gallagher, L.E., Radhi, O.A., Abdullah, M.O., McCluskey, A.G., Boyd, M., and Chan, E.Y.W. (2017). Lysosomotropism depends on glucose: a chloroquine resistance mechanism. Cell Death Dis. *8*, e3014.

Gomes, L.C., Di Benedetto, G., and Scorrano, L. (2011a). During autophagy mitochondria elongate, are spared from degradation and sustain cell viability. Nat. Cell Biol. *13*, 589–598.

Gomes, L.C., Di Benedetto, G., and Scorrano, L. (2011b). Essential amino acids and glutamine regulate induction of mitochondrial elongation during autophagy. Cell Cycle *10*, 2635–2639.

Gonzalez, G.A., and Montminy, M.R. (1989). Cyclic AMP stimulates somatostatin gene transcription by phosphorylation of CREB at serine 133. Cell *59*, 675–680.

Gravel, S.-P., Avizonis, D., and St-Pierre, J. (2016). Metabolomics analyses of cancer cells in controlled microenvironments. In The Tumor Microenvironment: Methods and Protocols, J. Ursini-Siegel and N. Beauchemin, eds. (Springer New York), pp. 273–290.

Harada, H., Becknell, B., Wilm, M., Mann, M., Huang, L.J., Taylor, S.S., Scott, J.D., and Korsmeyer, S.J. (1999). Phosphorylation and inactivation of BAD by mitochondria-anchored protein kinase A. Mol. Cell *3*, 413–422.

Head, B., Griparic, L., Amiri, M., Gandre-Babbe, S., and van der Bliek, A.M. (2009). Inducible proteolytic inactivation of OPA1 mediated by the OMA1 protease in mammalian cells. J. Cell Biol. *187*, 959–966.

Hoppins, S., Edlich, F., Cleland, M.M., Banerjee, S., McCaffery, J.M., Youle, R.J., and Nunnari, J. (2011). The soluble form of Bax regulates mitochondrial fusion via MFN2 homotypic complexes. Mol. Cell *41*, 150–160.

Hoxhaj, G., Hughes-Hallett, J., Timson, R.C., Ilagan, E., Yuan, M., Asara, J.M., Ben-Sahra, I., and Manning, B.D. (2017). The mTORC1 signaling network senses changes in cellular purine nucleotide levels. Cell Rep. *21*, 1331–1346.

Huang, F., Ni, M., Chalishazar, M.D., Huffman, K.E., Kim, J., Cai, L., Shi, X., Cai, F., Zacharias, L.G., Ireland, A.S., et al. (2018). Inosine monophosphate dehydrogenase dependence in a subset of small cell lung cancers. Cell Metab. *28*, 369–382.e5.

Ishihara, N., Fujita, Y., Oka, T., and Mihara, K. (2006). Regulation of mitochondrial morphology through proteolytic cleavage of OPA1. EMBO J. *25*, 2966–2977.

Ishihara, N., Nomura, M., Jofuku, A., Kato, H., Suzuki, S.O., Masuda, K., Otera, H., Nakanishi, Y., Nonaka, I., Goto, Y.I., et al. (2009). Mitochondrial fission factor Drp1 is essential for embryonic development and synapse formation in mice. Nat. Cell Biol. *11*, 958–966.

Ivosev, G., Burton, L., and Bonner, R. (2008). Dimensionality reduction and visualization in principal component analysis. Anal. Chem. *80*, 4933–4944.

Jewell, J.L., Kim, Y.C., Russell, R.C., Yu, F.X., Park, H.W., Plouffe, S.W., Tagliabracci, V.S., and Guan, K.L. (2015). Metabolism. Differential regulation of mTORC1 by leucine and glutamine. Science *347*, 194–198.

Ji, Y., Gu, J., Makhov, A.M., Griffith, J.D., and Mitchell, B.S. (2006). Regulation of the interaction of inosine monophosphate dehydrogenase with mycophenolic Acid by GTP. J. Biol. Chem. *281*, 206–212.

Kashatus, J.A., Nascimento, A., Myers, L.J., Sher, A., Byrne, F.L., Hoehn, K.L., Counter, C.M., and Kashatus, D.F. (2015). Erk2 phosphorylation of Drp1 promotes mitochondrial fission and MAPK-driven tumor growth. Mol. Cell *57*, 537–551.

Keshet, R., Szlosarek, P., Carracedo, A., and Erez, A. (2018). Rewiring urea cycle metabolism in cancer to support anabolism. Nat. Rev. Cancer *18*, 634–645.

Kirwan, G.M., Johansson, E., Kleemann, R., Verheij, E.R., Wheelock, Å.M., Goto, S., Trygg, J., and Wheelock, C.E. (2012). Building multivariate systems biology models. Anal. Chem. *84*, 7064–7071.

Kleele, T., Rey, T., Winter, J., Zaganelli, S., Mahecic, D., Perreten Lambert, H., Ruberto, F.P., Nemir, M., Wai, T., Pedrazzini, T., and Manley, S. (2021). Distinct fission signatures predict mitochondrial degradation or biogenesis. Nature *593*, 435–439.

Koshiba, T., Detmer, S.A., Kaiser, J.T., Chen, H., McCaffery, J.M., and Chan, D.C. (2004). Structural basis of mitochondrial tethering by mitofusin complexes. Science *305*, 858–862.

Kuma, A., Hatano, M., Matsui, M., Yamamoto, A., Nakaya, H., Yoshimori, T., Ohsumi, Y., Tokuhisa, T., and Mizushima, N. (2004). The role of autophagy during the early neonatal starvation period. Nature *432*, 1032–1036.

Kurmi, K., and Haigis, M.C. (2020). Nitrogen metabolism in cancer and immunity. Trends Cell Biol. *30*, 408–424.

Lackner, L.L., Horner, J.S., and Nunnari, J. (2009). Mechanistic analysis of a dynamin effector. Science *325*, 874.

Lane, A.N., and Fan, T.W.M. (2015). Regulation of mammalian nucleotide metabolism and biosynthesis. Nucleic Acids Res. *43*, 2466–2485.

Lebeau, J., Saunders, J.M., Moraes, V.W.R., Madhavan, A., Madrazo, N., Anthony, M.C., and Wiseman, R.L. (2018). The PERK arm of the unfolded protein response regulates mitochondrial morphology during acute endoplasmic reticulum stress. Cell Rep. *22*, 2827–2836.

Leboucher, G.P., Tsai, Y.C., Yang, M., Shaw, K.C., Zhou, M., Veenstra, T.D., Glickman, M.H., and Weissman, A.M. (2012). Stress-induced phosphorylation and proteasomal degradation of mitofusin 2 facilitates mitochondrial fragmentation and apoptosis. Mol. Cell *47*, 547–557.

Liao, L.X., Song, X.M., Wang, L.C., Lv, H.N., Chen, J.F., Liu, D., Fu, G., Zhao, M.B., Jiang, Y., Zeng, K.W., and Tu, P.F. (2017). Highly selective inhibition of IMPDH2 provides the basis of antineuroinflammation therapy. Proc. Natl. Acad. Sci. USA *114*, E5986–E5994.

McLelland, G.L., Soubannier, V., Chen, C.X., McBride, H.M., and Fon, E.A. (2014). Parkin and PINK1 function in a vesicular trafficking pathway regulating mitochondrial quality control. EMBO J. *33*, 282–295.

McLelland, G.L., Lee, S.A., McBride, H.M., and Fon, E.A. (2016). Syntaxin-17 delivers PINK1/parkin-dependent mitochondrial vesicles to the endolysosomal system. J. Cell Biol. *214*, 275–291.

Miret-Casals, L., Sebastián, D., Brea, J., Rico-Leo, E.M., Palacín, M., Fernández-Salguero, P.M., Loza, M.I., Albericio, F., and Zorzano, A. (2018). Identification of new activators of mitochondrial fusion reveals a link between mitochondrial morphology and pyrimidine metabolism. Cell Chem. Biol. *25*, 268–278.e4.

Mishra, P., Carelli, V., Manfredi, G., and Chan, D.C. (2014). Proteolytic cleavage of Opa1 stimulates mitochondrial inner membrane fusion and couples fusion to oxidative phosphorylation. Cell Metab. *19*, 630–641.

Mitra, K., Wunder, C., Roysam, B., Lin, G., and Lippincott-Schwartz, J. (2009). A hyperfused mitochondrial state achieved at G1-S regulates cyclin E buildup and entry into S phase. Proc. Natl. Acad. Sci. USA *106*, 11960–11965.

Morita, M., Prudent, J., Basu, K., Goyon, V., Katsumura, S., Hulea, L., Pearl, D., Siddiqui, N., Strack, S., McGuirk, S., et al. (2017). mTOR controls mitochondrial dynamics and cell survival via MTFP1. Mol. Cell *67*, 922–935.e5.

Nagdas, S., Kashatus, J.A., Nascimento, A., Hussain, S.S., Trainor, R.E., Pollock, S.R., Adair, S.J., Michaels, A.D., Sesaki, H., Stelow, E.B., et al. (2019). Drp1 promotes KRas-driven metabolic changes to drive pancreatic tumor growth. Cell Rep. *28*, 1845–1859.e5.

Nakada, K., Inoue, K., Ono, T., Isobe, K., Ogura, A., Goto, Y.I., Nonaka, I., and Hayashi, J.I. (2001). Inter-mitochondrial complementation: mitochondria-specific system preventing mice from expression of disease phenotypes by mutant mtDNA. Nat. Med. *7*, 934–940.

Naon, D., Zaninello, M., Giacomello, M., Varanita, T., Grespi, F., Lakshminaranayan, S., Serafini, A., Semenzato, M., Herkenne, S., Hernández-Alvarez, M.I., et al. (2016). Critical reappraisal confirms that Mitofusin 2 is an endoplasmic reticulum-mitochondria tether. Proc. Natl. Acad. Sci. USA *113*, 11249–11254.

Neuspiel, M., Schauss, A.C., Braschi, E., Zunino, R., Rippstein, P., Rachubinski, R.A., Andrade-Navarro, M.A., and McBride, H.M. (2008). Cargo-selected transport from the mitochondria to peroxisomes is mediated by vesicular carriers. Curr. Biol. *18*, 102–108.

Nunnari, J., Marshall, W.F., Straight, A., Murray, A., Sedat, J.W., and Walter, P. (1997). Mitochondrial transmission during mating in Saccharomyces cerevisiae is determined by mitochondrial fusion and fission and the intramitochondrial segregation of mitochondrial DNA. Mol. Biol. Cell *8*, 1233–1242.

Nwadike, C., Williamson, L.E., Gallagher, L.E., Guan, J.L., and Chan, E.Y.W. (2018). AMPK inhibits ULK1-dependent autophagosome formation and lysosomal acidification via distinct mechanisms. Mol. Cell Biol. *38*. e00023-18.

Ono, T., Isobe, K., Nakada, K., and Hayashi, J.I. (2001). Human cells are protected from mitochondrial dysfunction by complementation of DNA products in fused mitochondria. Nat. Genet. *28*, 272–275.

Pedley, A.M., and Benkovic, S.J. (2017). A new view into the regulation of purine metabolism: the purinosome. Trends Biochem. Sci. *42*, 141–154.

Pluskal, T., Castillo, S., Villar-Briones, A., and Oresic, M. (2010). MZmine 2: modular framework for processing, visualizing, and analyzing mass spectrometry-based molecular profile data. BMC Bioinformatics *11*, 395.

Prudent, J., Zunino, R., Sugiura, A., Mattie, S., Shore, G.C., and McBride, H.M. (2015). MAPL SUMOylation of Drp1 stabilizes an ER/mitochondrial platform required for cell death. Mol. Cell *59*, 941–955.

Pyakurel, A., Savoia, C., Hess, D., and Scorrano, L. (2015). Extracellular regulated kinase phosphorylates mitofusin 1 to control mitochondrial morphology and apoptosis. Mol. Cell *58*, 244–254.

Qi, X., Disatnik, M.H., Shen, N., Sobel, R.A., and Mochly-Rosen, D. (2011). Aberrant mitochondrial fission in neurons induced by protein kinase C{delta} under oxidative stress conditions in vivo. Mol. Biol. Cell *22*, 256–265.

Qi, Y., Yan, L., Yu, C., Guo, X., Zhou, X., Hu, X., Huang, X., Rao, Z., Lou, Z., and Hu, J. (2016). Structures of human mitofusin 1 provide insight into mitochondrial tethering. J. Cell Biol. *215*, 621–629.

Rambold, A.S., Kostelecky, B., Elia, N., and Lippincott-Schwartz, J. (2011a). Tubular network formation protects mitochondria from autophagosomal degradation during nutrient starvation. Proc. Natl. Acad. Sci. USA *108*, 10190–10195.

Rambold, A.S., Kostelecky, B., and Lippincott-Schwartz, J. (2011b). Together we are stronger: fusion protects mitochondria from autophagosomal degradation. Autophagy *7*, 1568–1569.

Rebsamen, M., Pochini, L., Stasyk, T., de Araújo, M.E.G., Galluccio, M., Kandasamy, R.K., Snijder, B., Fauster, A., Rudashevskaya, E.L., Bruckner, M., et al. (2015). SLC38A9 is a component of the lysosomal amino acid sensing machinery that controls mTORC1. Nature *519*, 477–481.

Sancak, Y., Thoreen, C.C., Peterson, T.R., Lindquist, R.A., Kang, S.A., Spooner, E., Carr, S.A., and Sabatini, D.M. (2007). PRAS40 is an insulin-regulated inhibitor of the mTORC1 protein kinase. Mol. Cell *25*, 903–915.

Sancak, Y., Bar-Peled, L., Zoncu, R., Markhard, A.L., Nada, S., and Sabatini, D.M. (2010). Ragulator-Rag complex targets mTORC1 to the lysosomal surface and is necessary for its activation by amino acids. Cell *141*, 290–303.

Serasinghe, M.N., Wieder, S.Y., Renault, T.T., Elkholi, R., Asciolla, J.J., Yao, J.L., Jabado, O., Hoehn, K., Kageyama, Y., Sesaki, H., and Chipuk, J.E. (2015). Mitochondrial division is requisite to RAS-induced transformation and targeted by oncogenic MAPK pathway inhibitors. Mol. Cell *57*, 521–536.

Shutt, T., Geoffrion, M., Milne, R., and McBride, H.M. (2012). The intracellular redox state is a core determinant of mitochondrial fusion. EMBO Rep. *13*, 909–915.

Son, S.M., Park, S.J., Lee, H., Siddiqi, F., Lee, J.E., Menzies, F.M., and Rubinsztein, D.C. (2019). Leucine signals to mTORC1 via its metabolite acetyl-coenzyme A. Cell Metab. *29*, 192–201.e7.

Song, Z., Chen, H., Fiket, M., Alexander, C., and Chan, D.C. (2007). OPA1 processing controls mitochondrial fusion and is regulated by mRNA splicing, membrane potential, and Yme1L. J. Cell Biol. *178*, 749–755.

Soubannier, V., McLelland, G.-L., Zunino, R., Braschi, E., Rippstein, P., Fon, E.A., and McBride, H.M. (2012). A vesicular transport pathway shuttles cargo from mitochondria to lysosomes. Curr. Biol. *22*, 135–141.

Spinelli, J.B., Yoon, H., Ringel, A.E., Jeanfavre, S., Clish, C.B., and Haigis, M.C. (2017). Metabolic recycling of ammonia via glutamate dehydrogenase supports breast cancer biomass. Science *358*, 941–946.

Sun, N., Youle, R.J., and Finkel, T. (2016). The mitochondrial basis of aging. Mol. Cell *61*, 654–666.

Taguchi, N., Ishihara, N., Jofuku, A., Oka, T., and Mihara, K. (2007). Mitotic phosphorylation of dynamin-related GTPase Drp1 participates in mitochondrial fission. J. Biol. Chem. *282*, 11521–11529.

Thoreen, C.C., Kang, S.A., Chang, J.W., Liu, Q., Zhang, J., Gao, Y., Reichling, L.J., Sim, T., Sabatini, D.M., and Gray, N.S. (2009). An ATP-competitive mammalian target of rapamycin inhibitor reveals rapamycin-resistant functions of mTORC1. J. Biol. Chem. *284*, 8023–8032.

Tomlinson, I.P.M., Alam, N.A., Rowan, A.J., Barclay, E., Jaeger, E.E.M., Kelsell, D., Leigh, I., Gorman, P., Lamlum, H., Rahman, S., et al. (2002). Germline mutations in FH predispose to dominantly inherited uterine fibroids, skin leiomyomata and papillary renal cell cancer. Nat. Genet. *30*, 406–410.

Tondera, D., Grandemange, S., Jourdain, A., Karbowski, M., Mattenberger, Y., Herzig, S., Da Cruz, S., Clerc, P., Raschke, I., Merkwirth, C., et al. (2009). SLP-2 is required for stress-induced mitochondrial hyperfusion. EMBO J. *28*, 1589–1600.

Towers, C.G., Wodetzki, D.K., Thorburn, J., Smith, K.R., Caino, M.C., and Thorburn, A. (2021). Mitochondrial-derived vesicles compensate for loss of LC3-mediated mitophagy. Dev. Cell *56*, 2029–2042.e5.

Twig, G., Elorza, A., Molina, A.J.A., Mohamed, H., Wikstrom, J.D., Walzer, G., Stiles, L., Haigh, S.E., Katz, S., Las, G., et al. (2008). Fission and selective fusion govern mitochondrial segregation and elimination by autophagy. EMBO J. *27*, 433–446.

Villar, V.H., Nguyen, T.L., Delcroix, V., Terés, S., Bouchecareilh, M., Salin, B., Bodineau, C., Vacher, P., Priault, M., Soubeyran, P., and Durán, R.V. (2017). mTORC1 inhibition in cancer cells protects from glutaminolysis-mediated apoptosis during nutrient limitation. Nat. Commun. *8*, 14124.

Wakabayashi, J., Zhang, Z., Wakabayashi, N., Tamura, Y., Fukaya, M., Kensler, T.W., Iijima, M., and Sesaki, H. (2009). The dynamin-related GTPase Drp1 is required for embryonic and brain development in mice. J. Cell Biol. *186*, 805–816.

Wasiak, S., Zunino, R., and McBride, H.M. (2007). Bax/Bak promote sumoylation of DRP1 and its stable association with mitochondria during apoptotic cell death. J. Cell Biol. *177*, 439–450.

Watson, D.G., Tonelli, F., Alossaimi, M., Williamson, L., Chan, E., Gorshkova, I., Berdyshev, E., Bittman, R., Pyne, N.J., and Pyne, S. (2013). The roles of sphingosine kinases 1 and 2 in regulating the Warburg effect in prostate cancer cells. Cell. Signal. *25*, 1011–1017.

Westermann, B. (2010). Mitochondrial fusion and fission in cell life and death. Nat. Rev. Mol. Cell Biol. *11*, 872–884.

Xia, J., and Wishart, D.S. (2010). MetPA: a web-based metabolomics tool for pathway analysis and visualization. Bioinformatics *26*, 2342–2344.

Xia, J., and Wishart, D.S. (2011). Metabolomic data processing, analysis, and interpretation using MetaboAnalyst. Curr. Protoc. Bioinformatics. Chapter 14, Unit 14.10.

Yan, L., Qi, Y., Huang, X., Yu, C., Lan, L., Guo, X., Rao, Z., Hu, J., and Lou, Z. (2018). Structural basis for GTP hydrolysis and conformational change of MFN1 in mediating membrane fusion. Nat. Struct. Mol. Biol. *25*, 233–243.

Yang, Y., Valera, V.A., Padilla-Nash, H.M., Sourbier, C., Vocke, C.D., Vira, M.A., Abu-Asab, M.S., Bratslavsky, G., Tsokos, M., Merino, M.J., et al. (2010). UOK 262 cell line, fumarate hydratase deficient (FH-/FH-) hereditary leiomyomatosis renal cell carcinoma: in vitro and in vivo model of an aberrant energy metabolic pathway in human cancer. Cancer Genet. Cytogenet. *196*, 45–55.

Yoshii, S.R., Kishi, C., Ishihara, N., and Mizushima, N. (2011). Parkin mediates proteasome-dependent protein degradation and rupture of the outer mitochondrial membrane. J. Biol. Chem. *286*, 19630–19640.

Chong, J., Soufan, O., Li, C., Caraus, I., Li, S., Bourque, G., Wishart, D.S., and Xia, J. (2018). MetaboAnalyst 4.0: towards more transparent and integrative metabolomics analysis. Nucleic Acids Res. *46*, W486–W494.

STAR★METHODS

KEY RESOURCES TABLE

REAGENT or RESOURCE	SOURCE	IDENTIFIER
Antibodies		
phospho-S6 serine 240/244	Cell Signaling	2215; RRID:AB_331682
phospho-ULK1 serine 757	Cell Signaling	6888; RRID:AB_10829226
total S6 (54D2)	Cell Signaling	2317; , RRID:AB_2238583
phospho-CREB serine 133	Cell Signaling	9198; RRID:AB_2561044
total CREB	Cell Signaling	9104; RRID:AB_490881
Actin (Ab-5)	BD Bioscience	612656; RRID:AB_2289199
Opa1	BD Bioscience	612606; RRID:AB_399888
Drp1 (DLP1)	BD Bioscience	611113; RRID:AB_398424
phospho-Drp1 serine 637 (Ab#1)	Cell signaling	6319; RRID:AB_10971640
phospho-Drp1 serine 637 (Ab#2)	Cell signaling	4867; RRID:AB_10622027
phospho-Drp1 serine 616	Cell signaling	4494; RRID:AB_11178659
Fumarase (D9C5)	Cell signaling	4567; RRID:AB_11178522
cleaved caspase 3 (Asp175) (5A1E)	Cell signaling	9664; RRID:AB_2070042
ATF-4 (D4B8)	Cell signaling	11815; RRID:AB_2616025
TOMM20	Santa Cruz Biotechnology	FL-145; RRID:AB_2207533
TOMM20	Abcam	EPR15581-54; RRID:AB_2889972
FGAMS (aka anti-PFAS)	Bethyl Laboratories	A304-218A; RRID:AB_2620415)
Chemicals, peptides, and recombinant proteins		
L-Glutamine (200mM)	Lonza Bioscience	BE17-605E
Earle's balanced salt solution (EBSS)	Sigma	E2888
DMEM, glucose-free (containing 4mM L-glutamine)	Thermo Fisher- Invitrogen Life Technologies	11966–025
DMEM, high glucose, no glutamine	Thermo Fisher- Invitrogen Life Technologies	11960–044
dialyzed FBS	Sigma	F0392
Leucine	Sigma	L8912
Arginine	Sigma	A8094
Isoleucine	Sigma	I2752
Valine	Sigma	V0500
Lysine	Sigma	L5501
Torin1	Tocris-Bio-Techne	4247
mycophenolic acid (MPA)	Tocris-Bio-Techne	1505
L-DON	Tocris-Bio-Techne	6809
Forskolin	Tocris-Bio-Techne	1099
Cycloheximide	Sigma	C7698
Guanosine	Sigma	G6264
mitotracker orange CMTM Ros	Thermo Fisher- Invitrogen Life Technologies	M7510
[13C5]-glutamine	Cambridge Isotopes	CLM-1822-H
[15N2]-glutamine	Cambridge Isotopes	NLM-1328
glutaraldehyde fixative	Sigma	G5882
HEPES pH 7.5 stock solution	Thermo Fisher- Invitrogen Life Technologies	15630–049

(*Continued on next page*)

Continued

REAGENT or RESOURCE	SOURCE	IDENTIFIER
Experimental models: Cell lines		
4T1 (Mouse breast cancer)	American Type Culture Collection (ATCC)	CRL-2539
HeLa (human cervical cancer)	American Type Culture Collection (ATCC)	CRM-CCL-2
U2OS (human osteosarcoma)	Cancer Research UK- London Research Institute - Central cell services	N/A
Matched wildtype and Atg5 KO MEF	provided by Noboru Mizushima (Kuma et al., 2004)	N/A
Matched wildtype and Opa1 KO MEF	obtained from Luca Scorrano, originally isolated by David Chan (Song et al., 2007).	N/A
Matched wildtype, Mfn1 KO, Mfn2 KO and Mfn1/2 double KO MEF	obtained from Luca Scorrano, originally isolated by David Chan (Chen et al., 2003; Koshiba et al., 2004)	N/A
Immortalized kidney cells conditionally targeted for fumarate hydratase 1 Fh1 (−/−) KO (clones 1 and 19) and (Fh1 fl/fl) control were obtained from Cancer Research UK Technology Limited	(Frezza et al., 2011).	N/A
UOK262 Fh (−/−) and UOK262-WT (re-constituted) cells	provided by W. M. Linehan (National Cancer Institute, Bethesda, USA) (Yang et al., 2010)	N/A
Recombinant DNA		
pMXs-IP-Su9-GFP	(Yoshii et al., 2011)	N/A
LKO-puro shRNA for mouse Drp1 (Dnm1l)	Dharmacon-Horizon Biosystems	TRCN0000012605
Software and algorithms		
ProteoWizard	(Chambers et al., 2012)	https://proteowizard.sourceforge.io/
Image Studio Lite	LI-COR biotechnology	https://www.licor.com/bio/image-studio-lite/
MZmine 2.10	MZmine (Pluskal et al., 2010)	http://mzmine.github.io/
MetaboAnalyst-4.0	(Chong et al., 2018)	https://www.metaboanalyst.ca/
Heatmapper	(Babicki et al., 2016)	http://www.heatmapper.ca/
Profinder	Agilent Technologies	N/A
GraphPad Prism 9	GraphPad Software	https://www.graphpad.com/scientific-software/prism/

RESOURCE AVAILABILITY

Lead contact

Further queries on resources and reagents should be directed to: Edmond Chan (eywc@queensu.ca).

Materials availability

This study did not generate new unique reagents.

Data and code availability

All data reported in this paper will be shared by the lead contact upon request.
This paper does not generate original code.
Any additional information required to reanalyze the data reported in this paper is available from the lead contact upon request.

EXPERIMENTAL MODEL ANS SUBJECT DETAILS

Cell culture and treatments

Mouse breast cancer cells (4T1) (Gallagher et al., 2017) and human cervical cancer cells (HeLa) (Nwadike et al., 2018) were described in our previous work. Further details on KO MEF and cell line models listed in Key resources table. Where indicated, 4T1 or U2OS cells were derived to stably express Su9-GFP (F0-ATPase subunit 9 fused to GFP) following retrovirus transduction and puromycin selection. Where indicated, 4T1 or wildtype MEF were transduced with LKO-puro shRNA contructs to stably silence Drp1 (Dnm1l).

All cells were maintained at 37°C in DMEM with high (4.5g/L) glucose (Lonza #BE12-614F) supplemented with 10% fetal bovine serum (FBS), 4mM L-Glutamine (Lonza #BE17-605E), and 100U/mL Penicillin/Streptomycin (Lonza #DE17-602E) (full-nutrient media). Cells were washed 1x with PBS and exchanged into starvation media. For amino acid starvation, we used Earle's balanced salt solution (EBSS). For glucose (and serum) starvation, we used glucose-free DMEM media containing 4mM L-Glutamine. Where indicated, dialyzed FBS was supplemented. Where indicated 4 mM glutamine, 0.8 mM leucine and 0.4 mM arginine were supplemented back into EBSS (to levels found in normal DMEM formulation). Other amino acids tested include: 0.8 mM isoleucine, 0.8 mM valine or 0.8 mM lysine. Amino acid stocks (except glutamine) were made from powder freshly dissolved in distilled water. For drug treatments, we used starvation media as above in the presence or absence of the following drugs; MTOR inhibitor Torin1, mycophenolic acid (MPA), L-DON, forskolin or cycloheximide. Where indicated in figure legends, drugs were added in context of full-nutrient basal media. Where indicated, guanosine was supplemented into cell culture media. Guanosine stocks were freshly prepared in DMSO and added to 20 μM (final concentration). For analysis of purinosomes, 4T1 cells were pre-conditioned under purine-depletion contexts by culture in DMEM, high glucose, no glutamine, supplemented with 1% penicillin/streptomycin, 10% dialyzed FBS for a minimum of 7 days before experiments.

METHOD DETAILS

Immunoblot analysis

Cell lysates were prepared after various treatments by first briefly washing in ice-cold PBS before lysing in TNTE buffer (20 mM Tris pH 7.4, 150 mM NaCl, 5 mM EDTA, 1% Triton X-100) supplemented with HALT protease inhibitor cocktail (ThermoFisher Sci). Clarified cell lysates with mixed with concentrated Laemmli buffer and samples were heated at 95°C (5 min) before being resolved on hand-poured 10% NuPAGE gels and electrophoresis using 1x MES buffer (Invitrogen Life Technologies). Proteins transferred onto PVDF (Immobilon-FL, Millipore) membranes were blocked with 5% milk/TBS and incubated with indicated primary antibodies according to manufacturer protocols. Typically antibodies from Cell Signaling were diluted 1/1000 in 5%BSA/TBS/0.1% Tween 20. Typically antibodies from BD Biosciences were diluted 1/500–1/5000 in TBS. Antibody binding took place overnight at 4°C. Detection was via anti-mouse or anti-rabbit Dylight-coupled secondary antibodies and Licor Odyssey infrared scanning. Quantification of immunoblot signals was carried out using Licor Image Studio Lite.

Microscopy

Cells were seeded on fibronectin-coated (for 4T1 cells) or uncoated (all other cell types) glass coverslips. After treatments, where indicated, mitochondria were stained during the last 30 min of incubation using mitotracker orange CMTMRos. Cells expressing Su9-GFP were visualised directly after fixation. Where indicated, cells were stained using the following antibodies: TOMM20 (FL-145) (or alternatively [EPR15581-54]); Drp1 or cleaved caspase 3. For analysis of purinosomes, cells were fixed and stained with FGAMS rabbit antibody (aka anti-PFAS) followed by incubation with anti-rabbit Alexa 488 secondary antibody. Following extensive washing, cells were next briefly incubated with Alexa 555-coupled anti-TOMM20 antibody [EPR15581-54]), before further washes and mounting on glass slides. Cell images were captured by confocal microscopy (Leica TCS SP5, HCX PL APO CS-63x-1.4NA objective coupled with HyD GaAsP detection; or Zeiss LSM 710, 63x-1.4NA Plan-APOCHROMAT).

Steady state metabolite analysis

For analysis of steady state levels, samples were derived from 1.0×10^6 4T1 cells seeded in 10cm plates. After treatments, cells were extracted with pre-cooled 80/20% HPLC-grade (methanol/water). Cleared extracts were stored at −80°C until analysis on a Thermo Scientific Orbitrap Q Exactive (LC-MS) with separation on a ZIC-pHILIC column (150 × 4.6mm, 5μm, HiChrom, Reading, UK): gradient mobile phase consisting of 20mM ammonium carbonate/water (pH 9.2) and acetonitrile (flow rate: 300μL/min) (Watson et al., 2013).

Stable isotope tracer analysis

Samples were derived from 0.8×10^6 4T1 cells seeded in 6cm plates. The following day, cells were rinsed in PBS and exchanged into labeling media comprised of EBSS starvation media containing isotope-labelled Q (4 mM final), L (0.8 mM) and R (0.4 mM). Isotope label was either [$^{13}C_5$]-Q or [$^{15}N_2$]-Q as we described previously (Gravel et al., 2016). At the indicated timepoints, incubations were stopped quenched by briefly rinsing cells with ice-cold ammonium formate (150 mM, pH 7.4) before extraction with pre-cooled 80/20% HPLC-grade (methanol/water) and stored at −80°C. Control samples were also prepared with natural abundance glutamine to check for potential ion interference. Six 1.4 mm ceramic beads were added to each sample. Samples were bead-beat for 2m at 30 Hz and cleared by centrifugation. Clarified supernatant was transferred to a fresh pre-cooled tube and dried by vacuum centrifugation with sample temperature maintained at −4°C (Labconco, Kansas City MO, USA). Samples were resuspended in 50 μL UPLC grade water, clarified by centrifugation at 1°C and transferred to LC/MS vials with 200 μL inserts. A volume of 5 μL was injected for stable isotope tracer analysis onto an Agilent 6530 quadrupole time of flight (QTOF) mass spectrometer. Chromatographic separation of metabolites was achieved by using a 1290 Infinity ultra-performance liquid chromatography system (Agilent Technologies). Eluent ionization was achieved using Agilent Jet stream electrospray ionization. The source-gas temperature and flow were set at

150°C and 13 L m^{-1}, respectively. The nebulizer pressure was set at 45 psi and capillary voltage was set at 2000 V. Eluents were detected using negative ionization.

Chromatographic resolution of metabolites was achieved using a Zorbax Extend C18 column 1.8 μm, 2.1 × 150mm^2 with guard column 1.8 μm, 2.1 × 5mm^2 (Agilent Technologies). The gradient started at 100% mobile phase A (97% water, 3% methanol, 10 mM tributylamine, 15 mM acetic acid, 5 μM medronic acid) for 2.5m, followed with a 5m gradient to 20% mobile phase B (methanol, 10 mM tributylamine, 15 mM acetic acid, 5 μM medronic acid), a 5.5m gradient to 45% mobile phase C (90% ACN) and a 7m gradient to 99% B at a flow rate of 0.25 mL m^{-1}. This was followed by a 4m hold time at 100% mobile phase B. The column was restored by back-washing with 99% mobile phase C for 3m at 0.25 mL m^{-1}, followed by increase of the flow rate to 0.8 mL m^{-1} over 0.5m and a 3.85m hold, after which the flow rate was decreased to 0.6 mL m^{-1} over 0.15m. The column was re-equilibrated at 100% A over 0.75m, during which the flow rate was decreased to 0.4 mL m^{-1}, and held for 7.65m. One minute before the next injection, the flow was brought back to forward flow at 0.25 mL m^{-1}. The column temperature was maintained at 35°C. Retention times and linear range of detection were obtained by running authentic standard mixes which were injected repeatedly throughout the run to monitor analyte retention time and chromatographic quality.

Transmission electron microscopy

4T1 cells after treatment were fixed in 2% glutaraldehyde diluted in 0.2 M HEPES pH 7.5 for 2 h at room temperature and stored in 0.2 M HEPES without fixative at 4°C. Image acquisition was performed as described (Anwar et al., 2019) using a JEM-1400 Plus (Jeol Ltd, Tokyo, Japan) transmission electron microscope (primary magnification: 5000×).

QUANTIFICATION AND STATISTICAL ANALYSIS

To quantity mitochondrial sizes, five to ten confocal images (using 63x objectives, 1.40NA) typically were acquired per coverslip. Mitochondrial length was quantified from images using free-hand line tool in ImageJ traced onto the distended maximal length of a clearly visible mitochondrion. Ten mitochondrial lengths were quantified and averaged to calculate mean mitochondrial length per cell. The number of cells quantified was typically 40–50 per sample. Pooled datasets typically contained at least N = 3 biological replicates representing at minimum 2 independent experiments as detailed in legends. Each treatment group in mitochondrial length graphs indicate mean ± SD, plotted as relative units. For consistency, mitochondrial size results from different experiments/different cell systems are presented as fold change relative to a control response (e.g. full amino acid starvation). All replicates for a given experiment had the same normalisation applied and details are specified in figure legends. Mitochondria for quantification were chosen randomly within the cytosol with morphology clarity being the major criteria. Collapsed mitochondria that could not be classified as a distinct structure were avoided (e.g collapsed mitochondria close to nuclei). To limit bias, some experiments were blind coded before quantification. Notable, the QLR-hyperfusion response was blindly confirmed on multiple occasions. Cleaved caspase 3 puncta were counted from representative images.

For steady state metabolite analyses, data processing involved separation into positive or negative ionisation mode signals using the msconvert tool in ProteoWizard before analysis using MZmine 2.10. For identification of metabolites, peak lists were screened through a database containing metabolites mass data from the human metabolome, Kyoto Encyclopedia of Genes and Genomes (KEGG), Lipidmaps, MetaCyc and Metlin databases (Creek et al., 2012). Peak quality and retention time was crosschecked with a set of metabolite standards run via ZIC-pHILIC. The peak intensities of each metabolite (without data normalization) were uploaded to MetaboAnalyst-4.0 for principal component analysis (PCA). Data subsets listing metabolites identified by t test as altered $p < 0.05$ (comparing –AA vs. QLR-addback) were tested in MetaboAnalyst for Pathway enrichment and Over representation (hypergeometric) analysis. Metabolite cluster analysis was performed via Heatmapper.

For stable isotope tracer studies, area under the curve for each sample and metabolite and associated isotopes were analyzed and ensured to be below the saturation limit. No corrections were made for ion suppression effects. Stable isotope tracer data were analyzed and matrix correction performed using Profinder software. Experimental cell samples were exposed to ^{13}C- or ^{15}N-labeled Q and control samples exposed to equivalent natural abundance Q were analyzed in parallel to ensure that observed ^{13}C- or ^{15}N-incorporation into other metabolites were not due to interfering ions.

Quantitative data were managed using GraphPad Prism and typically analyzed using one-way ANOVA with Bonferroni post-test (multiple comparisons) or unpaired T test (for 2-way comparisons) as appropriate (further detailed in figure legends). Significance (calculated to 4 decimal points) was denoted in output style of GraphPad as: (*) $p < 0.05$; (**) $p < 0.01$; (***) $p < 0.001$; (****) $p < 0.0001$.

Cell Reports, Volume *40*

Supplemental information

Mitochondrial hyperfusion via metabolic sensing of regulatory amino acids

Mahmud O. Abdullah, Run X. Zeng, Chelsea L. Margerum, David Papadopoli, Cian Monnin, Kaylee B. Punter, Charles Chu, Mohammad Al-Rofaidi, Naser F. Al-Tannak, Domenica Berardi, Zahra Rattray, Nicholas J.W. Rattray, Sheela A. Abraham, Eeva-Liisa Eskelinen, David G. Watson, Daina Avizonis, Ivan Topisirovic, and Edmond Y.W. Chan

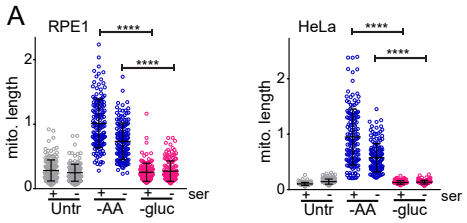

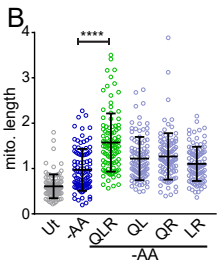

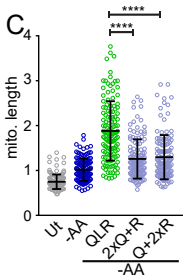

F

mouse pLKO shRNA Dnm1l (Drp1) clone data

code	clone ID	target sequence	intrinsic score
a	TRCN0000012604	GCCAACTGGATATTAACAATA	13.200
b	TRCN0000012605	GCTTCAGATCAGAGAACTTAT	13.200
c	TRCN0000012606	CGGTGGTGCTAGGATTTGTTA	5.625
d	TRCN0000012607	CCTGCTTTATTTGTGCCTGAA	4.050

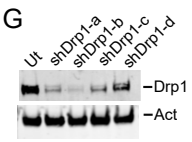

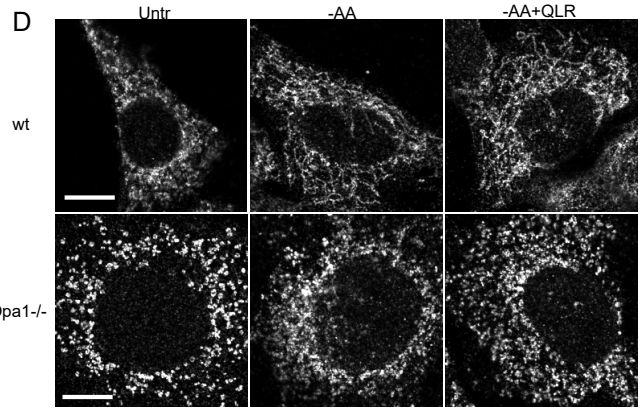

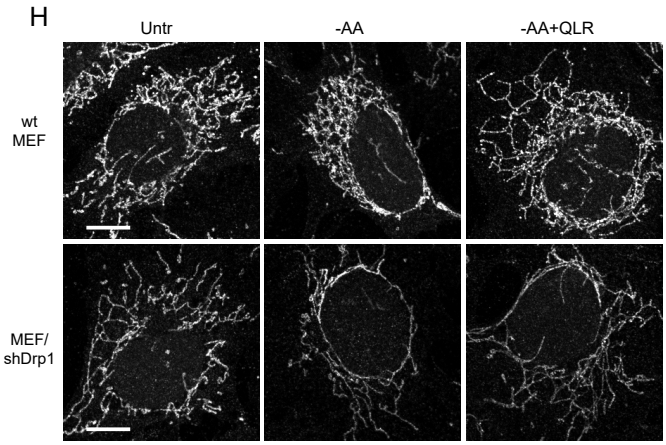

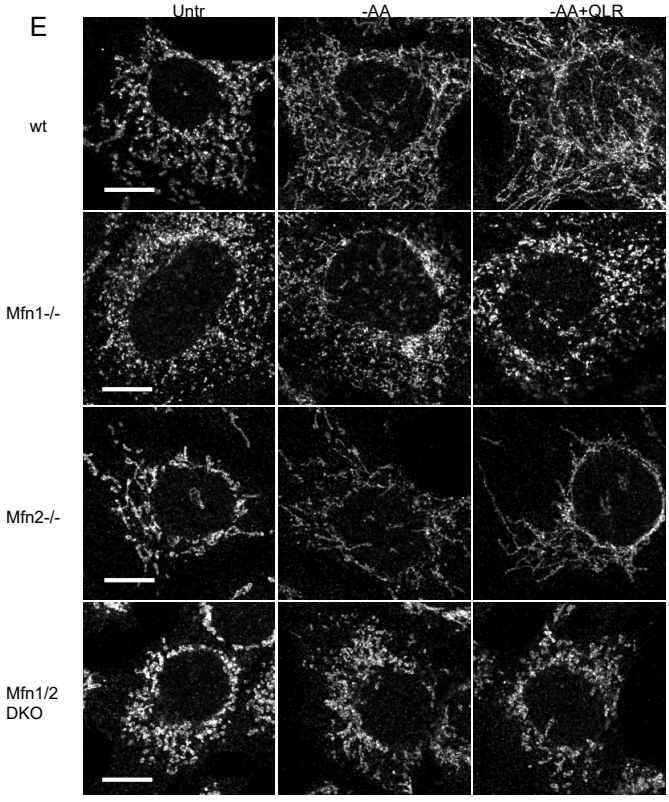

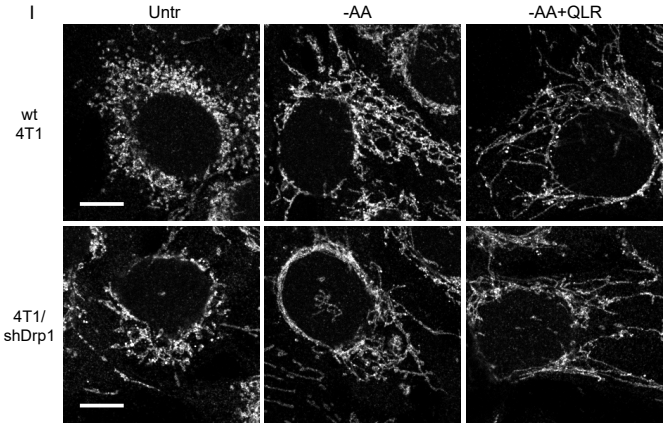

Figure S1

Figure S1: Regulation of mitochondrial hyperfusion by amino acid levels and requirement for canonical fusion factors. Related to Figure 1.

(A) Human RPE1 or HeLa cells were incubated under full-nutrients as untreated control (Untr) or starved of amino acids (-AA). Starvation was for: RPE1 (4h) or HeLa (24h). Mitochondria were visualised by staining TOMM20. Quantification of mitochondrial length in cells starved of amino acid or glucose (-gluc) in combination with serum starvation. Each treatment shows 150 cells quantified from 3 experiments represented as arbitrary units relative to amino acid starvation (in presence of serum) as 1.

(B) 4T1/Su9GFP cells were incubated in amino acid starvation media containing addback with different amino acid combinations as indicated for 4h. Final concentrations of supplemented amino acids: Q (4 mM), L (0.8 mM), R (0.4 mM). Cells were analysed for mitochondrial length (arbitrary units relative to amino acid starvation as 1). Each treatment shows 100 cells quantified from 4 experiments.

(C) 4T1 cells were incubated in amino acid starvation media containing addback with different amino acid combinations as indicated for 4h. Combinations included 2XQ+R (Q: 8 mM; R: 0.4 mM) and Q+2xR (Q: 4 mM; R: 0.8 mM). Cells were stained with Mitotracker orange and analysed for mitochondrial length (arbitrary units relative to amino acid starvation as 1). Each treatment shows 120 cells quantified from 3 experiments. (A-C) Mitochondrial quantification plots show mean +/- S.D.

(D) Matched wildtype (wt) or Opa1 (-/-) null MEF were incubated under full-nutrients (untreated, Untr), starved of either all amino acids (-AA) or incubated in starvation medium supplemented with glutamine (Q), leucine (L) and arginine (R) together for 4h. Starvation media conditions contained 10% dialysed FBS.

(E) Experiment as in (D) for matched wildtype, Mfn1(-/-), Mfn2(-/-), and Mfn1/2 double KO null MEF.

(F) Information on shRNA clones tested for mouse Drp1 (BROAD Institute Genetic Perturbation Platform).

(G) Knockdown efficiency confirmed by stable expression of LKO shRNA vectors in wt MEF. shDrp1-b was chosen for remainder of experiments.

(H,I) MEF or 4T1 stably expressed shDrp1-b and were incubated under full-nutrients (Untr), starved of either all amino acids (-AA) or incubated in starvation medium supplemented with glutamine (Q), leucine (L) and arginine (R) together for 4h.

All starvation conditions (except in S1A) contained 10% dialysed FBS. Comparisons analysed by one way ANOVA, Bonferroni post test. (***) $P<0.001$; (****) $P<0.0001$. All scale bars: 10 μm.

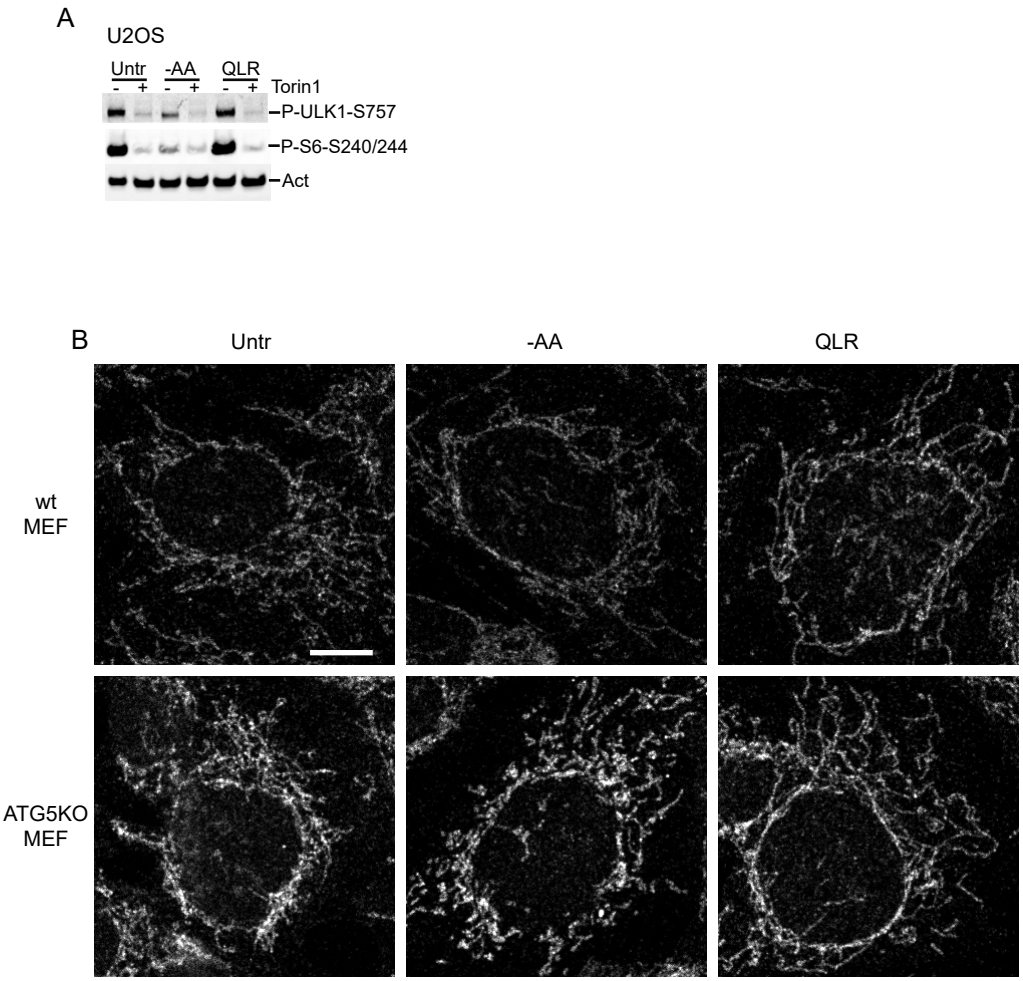

Figure S2: Amino acid supplementation re-activates MTORC1 signalling and promotes mitochondrial hyperfusion independently of autophagy. Related to Figure 2.

(A) U2OS/Su9GFP cells were fully starved of amino acids (-AA) or incubated in EBSS starvation medium supplemented with QLR +/- Torin1 (0.25μM) for 4h. Starvation media conditions contained 10% dialysed FBS. Protein extracts were tested for MTORC1 activity by immunoblotting phosphorylation of downstream substrates ULK1-Ser757 and S6.

(B) Matched wildtype (wt) or ATG5KO (-/-) MEF were incubated under full-nutrients (Untr), starved of either all amino acids (-AA) or incubation in starvation medium supplemented with glutamine (Q), leucine (L) and arginine (R) together for 4h. Starvation media conditions contained 10% dialysed FBS. Scale bar 10 μm.

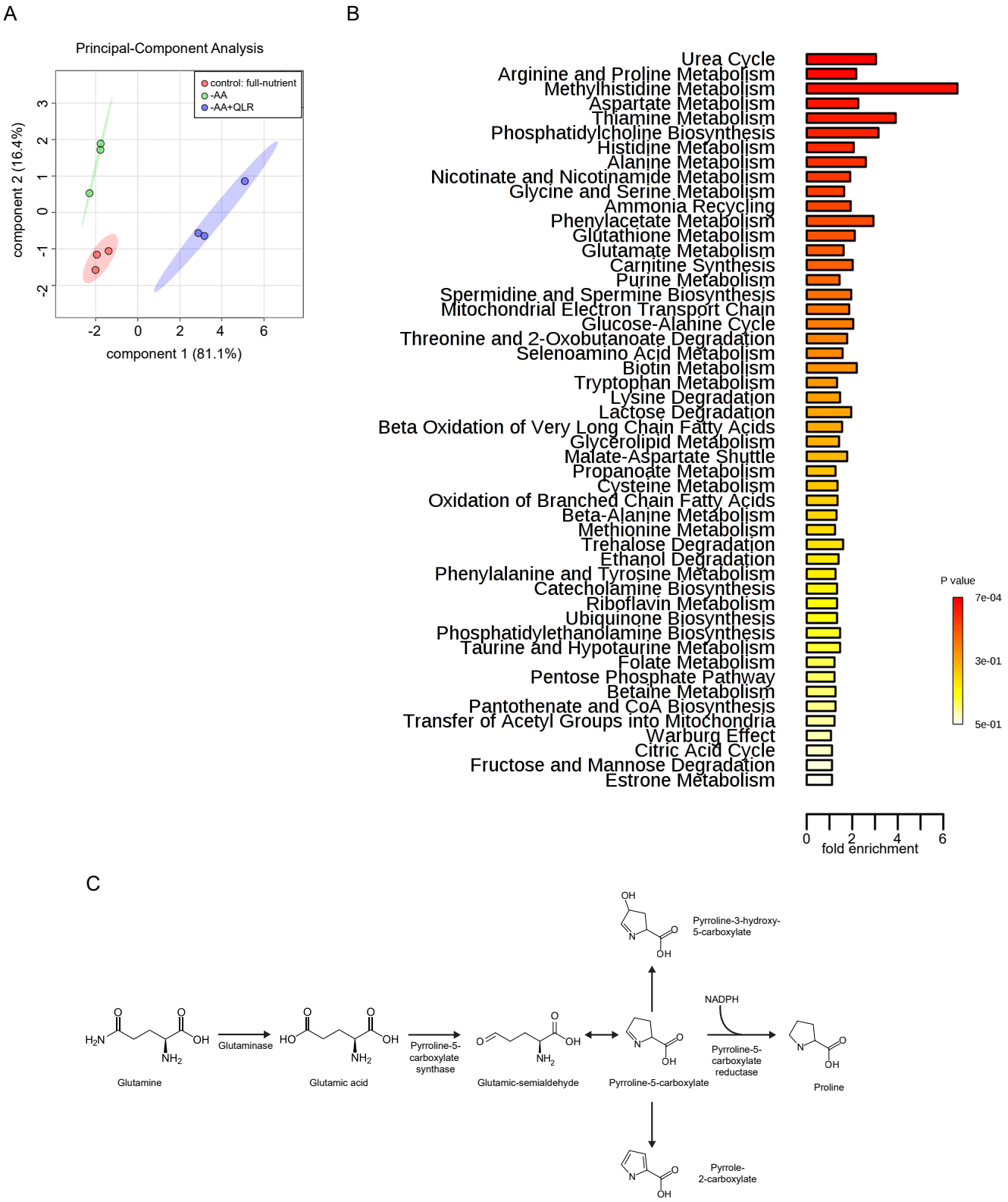

Figure S3. QLR supplementation leads to metabolic reprogramming of amino acid and nucleotide pathways. Related to Figure 3.

(A) 4T1 cells were incubated in control full nutrient conditions; under amino acid starvation (-AA); or in starvation media supplemented with QLR for 4h. Starvation conditions contained 10% dialysed FBS. Extracts were analysed by LC-MS. Principle component analysis is shown. PC1 shows approximately 5x greater variance relative to PC2 (comparing -AA vs QLR). N=3 replicates per condition.

(B) Enrichment overview (top 50) from Over Representation Analysis of LC-MS metabolite data when comparing -AA vs QLR addback conditions (analysis using MetaboAnalyst 4.0 suite).

(C) Proline biosynthetic pathway highlighting intermediate pyrroline-5-carboxylate and derivatives.

4T1 cells maintained in DMEM before experiment

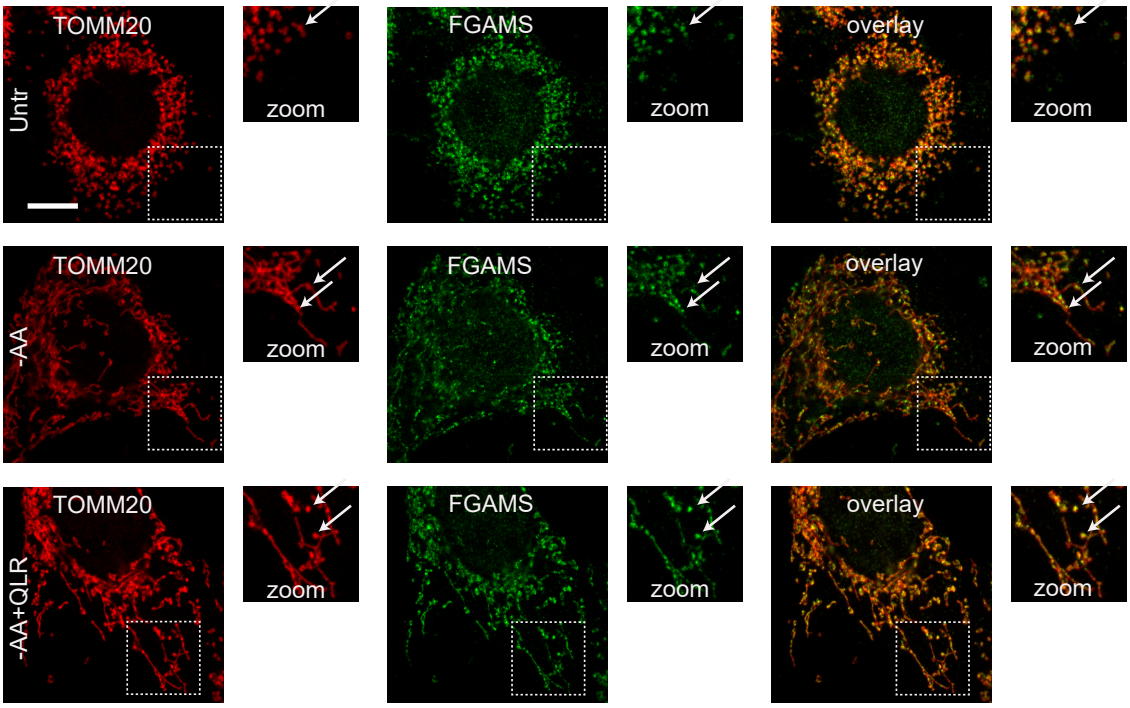

Figure S4. FGAMS(+) purinosomes remain associated on mitochondria following QLR-supplementation. Related to Figure 4

4T1 cells (maintained under normal purine-replete culture conditions, no-pre-conditioning) were tested as indicated for 4 h. Starvation conditions contained 10% dialysed FBS. Cells were stained for TOMM20 and FGAMS. Zoomed inset: Arrows highlight examples of colocalisation. Scale bar 10 μm.

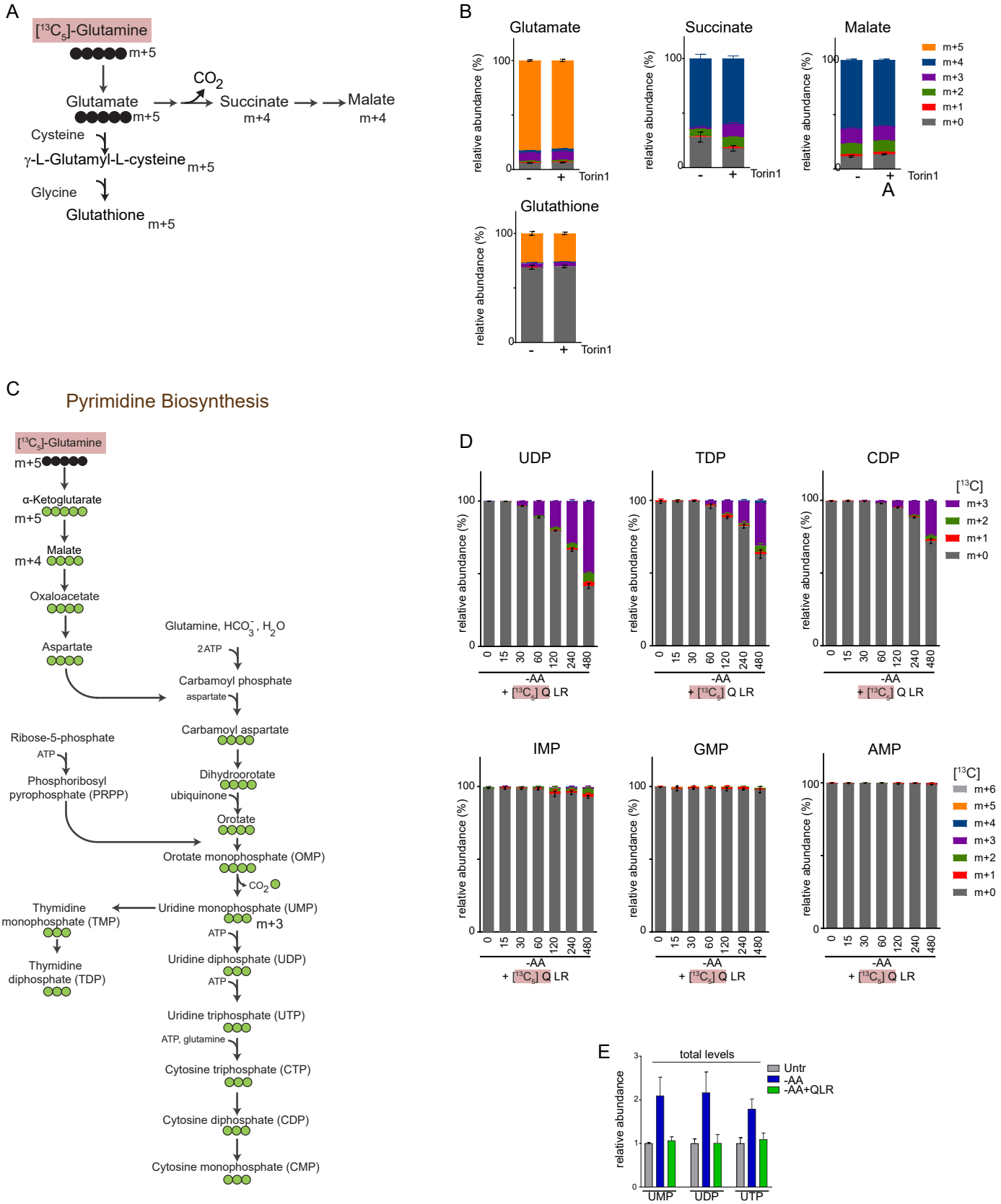
A
[13C5]-Glutamine
m+5
Glutamate
m+5
CO2
Succinate
m+4
Malate
m+4
Cysteine
γ-L-Glutamyl-L-cysteine
m+5
Glycine
Glutathione
m+5
B
Glutamate
Succinate
Malate
relative abundance (%)
100
0
- + Torin1
m+5
m+4
m+3
m+2
m+1
m+0
A
Glutathione
C
Pyrimidine Biosynthesis
[13C5]-Glutamine
m+5
α-Ketoglutarate
m+5
Malate
m+4
Oxaloacetate
Aspartate
Glutamine, HCO3-, H2O
2 ATP
Carbamoyl phosphate
aspartate
Carbamoyl aspartate
Ribose-5-phosphate
ATP
Phosphoribosyl pyrophosphate (PRPP)
Dihydroorotate
ubiquinone
Orotate
Orotate monophosphate (OMP)
CO2
Thymidine monophosphate (TMP)
Uridine monophosphate (UMP)
m+3
ATP
Thymidine diphosphate (TDP)
Uridine diphosphate (UDP)
ATP
Uridine triphosphate (UTP)
ATP, glutamine
Cytosine triphosphate (CTP)
Cytosine diphosphate (CDP)
Cytosine monophosphate (CMP)
D
UDP
TDP
CDP
IMP
GMP
AMP
relative abundance (%)
100
0
0 15 30 60 120 240 480
-AA
+ [13C5] Q LR
[13C]
m+6
m+5
m+4
m+3
m+2
m+1
m+0
E
total levels
relative abundance
3
2
1
0
UMP
UDP
UTP
Untr
-AA
-AA+QLR

Figure S5

Figure S5: Incorporation of ^{13}C-Glutamine into cellular intermediates is MTOR-independent and can supply pyrimidine biosynthesis. Related to Figure 5

(A) Schematic of stable isotope tracing into TCA cycle and related intermediates using [U-^{13}C]-Glutamine (Q).

(B) 4T1 cells were incubated in amino acid starvation + QLR supplementation conditions (containing [U-^{13}C]-Q) for 4h. Incubations were in the absence or presence of Torin1 (0.25 μM). Starvation conditions contained 10% dialysed FBS. Levels of indicated metabolites were determined by LC-MS. Data shown represent isotopologue levels: avg+/- S.D. from N=5 replicates.

(C) Schematic of stable isotope tracing into pyrimidine biosynthesis using [U-^{13}C]-Glutamine (Q).

(D) 4T1 cells were incubated in amino acid starvation + QLR supplementation conditions (containing [U-^{13}C]-Q) for 0 to 8h. Starvation conditions contained 10% dialysed FBS. Levels of representative metabolites in pyrimidine vs. purine biosynthesis pathways were determined by GC-MS. Data represent N=3 replicates per condition, avg +/- S.D. shown.

(E) Steady state levels of purine metabolites in 4T1 cells under amino acid starvation (-AA) or in starvation media supplemented with QLR for 4h (related to Main Figure 3). Starvation conditions contained 10% dialysed FBS. N=3 replicates per condition. Avg +/-SEM shown.

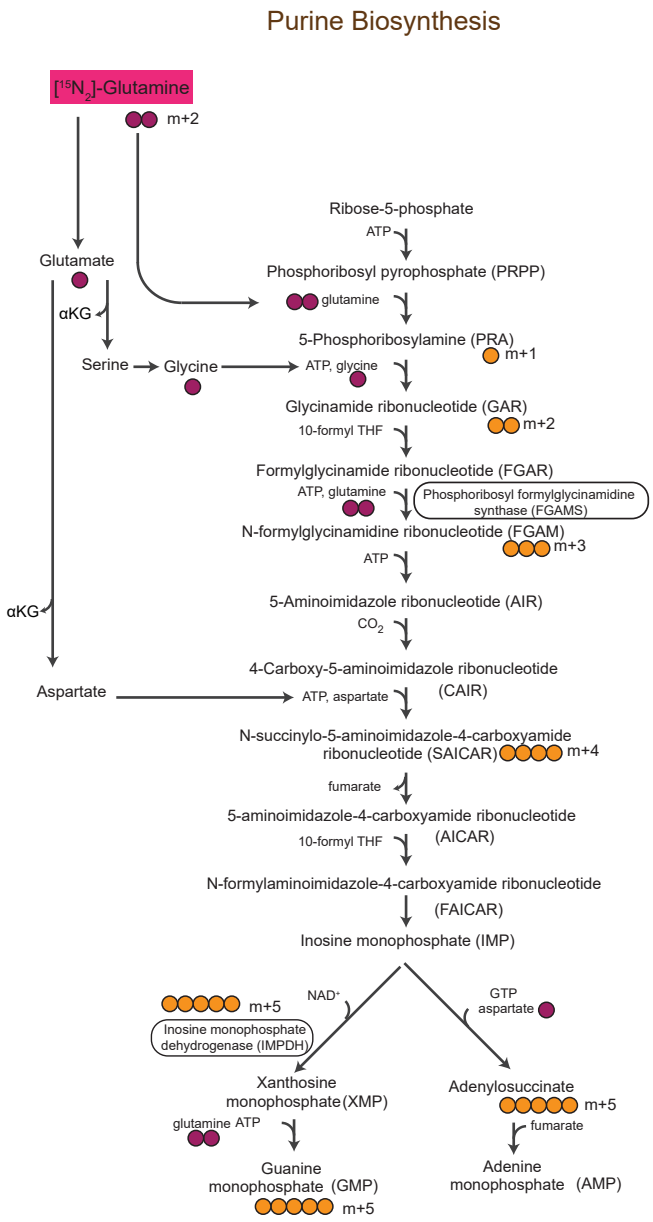

Figure S6. ^{15}N-Glutamine serves as nitrogen donor for purine biosynthesis. Related to Figure 5.

(A) Schematic of stable isotope tracing into the de novo purine biosynthesis pathway using double labeled [^{15}N-2]-Glutamine (Q). Key steps catalysed by enzymes FGAMS and IMPDH are highlighted.

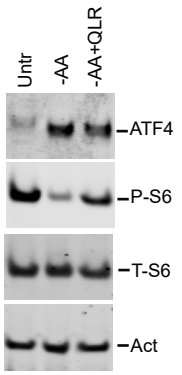

Figure S7. QLR-supplementation mitochondrial hyperfusion conditions are not associated with ATF4 activation. Related to Figure 6

4T1 cells were incubated in amino acid starvation + QLR supplementation conditions as indicated for 4h. Starvation conditions contained 10% dialysed FBS. Cell lysates were analysed by immunoblot.

Pathway	Total	Expected	Hits	raw-P	FDR
Urea Cycle	29	3.29	10	7.34E-04	7.19E-02
Arginine and Proline Metabolism	53	6.00	13	4.20E-03	1.70E-01
Methylhistidine Metabolism	4	0.45	3	5.21E-03	1.70E-01
Aspartate Metabolism	35	3.96	9	1.24E-02	2.42E-01
Thiamine Metabolism	9	1.02	4	1.25E-02	2.42E-01
Phosphatidylcholine Biosynthesis	14	1.59	5	1.48E-02	2.42E-01
Histidine Metabolism	43	4.87	10	1.75E-02	2.45E-01
Alanine Metabolism	17	1.93	5	3.46E-02	4.24E-01
Nicotinate and Nicotinamide Metabolism	37	4.19	8	4.87E-02	5.30E-01
Glycine and Serine Metabolism	59	6.68	11	5.98E-02	5.37E-01
Ammonia Recycling	32	3.62	7	6.03E-02	5.37E-01
Phenylacetate Metabolism	9	1.02	3	7.15E-02	5.84E-01
Glutathione Metabolism	21	2.38	5	7.88E-02	5.94E-01
Glutamate Metabolism	49	5.55	9	9.18E-02	6.08E-01
Carnitine Synthesis	22	2.49	5	9.31E-02	6.08E-01
Purine Metabolism	74	8.38	12	1.20E-01	7.35E-01
Spermidine and Spermine Biosynthesis	18	2.04	4	1.37E-01	7.90E-01
Mitochondrial Electron Transport Chain	19	2.15	4	1.59E-01	8.67E-01
Glucose-Alanine Cycle	13	1.47	3	1.75E-01	8.94E-01
Threonine and 2-Oxobutanoate Degradation	20	2.27	4	1.83E-01	8.94E-01
Selenoamino Acid Metabolism	28	3.17	5	2.03E-01	9.40E-01
Biotin Metabolism	8	0.91	2	2.27E-01	9.40E-01
Tryptophan Metabolism	60	6.80	9	2.30E-01	9.40E-01
Lysine Degradation	30	3.40	5	2.46E-01	9.40E-01
Lactose Degradation	9	1.02	2	2.71E-01	9.40E-01
Beta Oxidation of Very Long Chain Fatty Acids	17	1.93	3	3.01E-01	9.40E-01
Glycerolipid Metabolism	25	2.83	4	3.12E-01	9.40E-01
Malate-Aspartate Shuttle	10	1.13	2	3.16E-01	9.40E-01
Propanoate Metabolism	42	4.76	6	3.37E-01	9.40E-01
Cysteine Metabolism	26	2.95	4	3.39E-01	9.40E-01
Oxidation of Branched Chain Fatty Acids	26	2.95	4	3.39E-01	9.40E-01
Beta-Alanine Metabolism	34	3.85	5	3.39E-01	9.40E-01
Methionine Metabolism	43	4.87	6	3.59E-01	9.40E-01
Trehalose Degradation	11	1.25	2	3.59E-01	9.40E-01
Ethanol Degradation	19	2.15	3	3.67E-01	9.40E-01
Phenylalanine and Tyrosine Metabolism	28	3.17	4	3.94E-01	9.40E-01
Catecholamine Biosynthesis	20	2.27	3	3.99E-01	9.40E-01
Riboflavin Metabolism	20	2.27	3	3.99E-01	9.40E-01
Ubiquinone Biosynthesis	20	2.27	3	3.99E-01	9.40E-01
Phosphatidylethanolamine Biosynthesis	12	1.36	2	4.02E-01	9.40E-01
Taurine and Hypotaurine Metabolism	12	1.36	2	4.02E-01	9.40E-01
Folate Metabolism	29	3.29	4	4.21E-01	9.40E-01
Pentose Phosphate Pathway	29	3.29	4	4.21E-01	9.40E-01
Betaine Metabolism	21	2.38	3	4.31E-01	9.40E-01
Pantothenate and CoA Biosynthesis	21	2.38	3	4.31E-01	9.40E-01
Transfer of Acetyl Groups into Mitochondria	22	2.49	3	4.63E-01	9.86E-01
Warburg Effect	58	6.57	7	4.92E-01	1.00E+00
Citric Acid Cycle	32	3.62	4	5.00E-01	1.00E+00
Fructose and Mannose Degradation	32	3.62	4	5.00E-01	1.00E+00
Estrone Metabolism	24	2.72	3	5.23E-01	1.00E+00
Amino Sugar Metabolism	33	3.74	4	5.25E-01	1.00E+00
Phytanic Acid Peroxisomal Oxidation	26	2.95	3	5.80E-01	1.00E+00
Phosphatidylinositol Phosphate Metabolism	17	1.93	2	5.91E-01	1.00E+00
Pyruvate Metabolism	48	5.44	5	6.52E-01	1.00E+00
Butyrate Metabolism	19	2.15	2	6.54E-01	1.00E+00
De Novo Triacylglycerol Biosynthesis	9	1.02	1	6.63E-01	1.00E+00
Homocysteine Degradation	9	1.02	1	6.63E-01	1.00E+00
Pyrimidine Metabolism	59	6.68	6	6.78E-01	1.00E+00
Lactose Synthesis	20	2.27	2	6.82E-01	1.00E+00
Nucleotide Sugars Metabolism	20	2.27	2	6.82E-01	1.00E+00
Sphingolipid Metabolism	40	4.53	4	6.83E-01	1.00E+00
Tyrosine Metabolism	72	8.16	7	7.30E-01	1.00E+00
Sulfate/Sulfite Metabolism	22	2.49	2	7.33E-01	1.00E+00
Cardiolipin Biosynthesis	11	1.25	1	7.35E-01	1.00E+00
Degradation of Superoxides	11	1.25	1	7.35E-01	1.00E+00
Glycerol Phosphate Shuttle	11	1.25	1	7.35E-01	1.00E+00
Gluconeogenesis	35	3.96	3	7.79E-01	1.00E+00
Thyroid hormone synthesis	13	1.47	1	7.93E-01	1.00E+00
Glycolysis	25	2.83	2	7.96E-01	1.00E+00
Inositol Phosphate Metabolism	26	2.95	2	8.14E-01	1.00E+00
Vitamin K Metabolism	14	1.59	1	8.16E-01	1.00E+00
Mitochondrial Beta-Oxidation of Medium Chain Saturated Fatty Acids	27	3.06	2	8.31E-01	1.00E+00
Mitochondrial Beta-Oxidation of Short Chain Saturated Fatty Acids	27	3.06	2	8.31E-01	1.00E+00
Valine, Leucine and Isoleucine Degradation	60	6.80	5	8.32E-01	1.00E+00
Mitochondrial Beta-Oxidation of Long Chain Saturated Fatty Acids	28	3.17	2	8.46E-01	1.00E+00
Phospholipid Biosynthesis	29	3.29	2	8.60E-01	1.00E+00
Pterine Biosynthesis	29	3.29	2	8.60E-01	1.00E+00
Starch and Sucrose Metabolism	31	3.51	2	8.84E-01	1.00E+00
Inositol Metabolism	33	3.74	2	9.05E-01	1.00E+00
Vitamin B6 Metabolism	20	2.27	1	9.12E-01	1.00E+00
Steroid Biosynthesis	48	5.44	3	9.25E-01	1.00E+00
Galactose Metabolism	38	4.30	2	9.43E-01	1.00E+00
Androstenedione Metabolism	24	2.72	1	9.46E-01	1.00E+00
Bile Acid Biosynthesis	65	7.36	4	9.51E-01	1.00E+00
Plasmalogen Synthesis	26	2.95	1	9.58E-01	1.00E+00
Fatty acid Metabolism	43	4.87	2	9.66E-01	1.00E+00
Androgen and Estrogen Metabolism	33	3.74	1	9.82E-01	1.00E+00
Fatty Acid Elongation In Mitochondria	35	3.96	1	9.86E-01	1.00E+00
Retinol Metabolism	37	4.19	1	9.89E-01	1.00E+00
Steroidogenesis	43	4.87	1	9.95E-01	1.00E+00
Arachidonic Acid Metabolism	69	7.82	2	9.98E-01	1.00E+00

Table S1

Table S1: QLR supplementation leads to metabolic reprogramming. Related to Figure 3

Over Representation Analysis data from 4T1 / QLR addback experiment (detailed in: main Figure 5 and Supplemental Figure S5) comparing -AA vs QLR addback conditions (analysis using MetaboAnalyst 4.0). Number of Hits vs number expected as a measure of Over Representation.